SCIEPublish

Review

Photocatalytic Aerobic Conversion of Methane

Yuxiang Kong [1], Chunxiang Yang [1], Yiyu Cai [2], Xiaowei Mu [3,*] and Lu Li [1,*]

[1] State Key Laboratory of Inorganic Synthesis and Preparative Chemistry, College of Chemistry, Jilin University, Changchun 130012, China; kongyx22@mails.jlu.edu.cn (Y.K.); yangcx23@mails.jlu.edu.cn (C.Y.)

[2] Macao Institute of Materials Science and Engineering (MIMSE), Faculty of Innovation Engineering, Macau University of Science and Technology, Taipa, Macau SAR 999078, China; yycai@must.edu.mo (Y.C.)

[3] State Key Laboratory of Rare Earth Resource Utilization, Changchun Institute of Applied Chemistry, Changchun 130022, China

* Corresponding author. E-mail: muxw@ciac.ac.cn (X.M.); luli@jlu.edu.cn (L.L.)

Received: 28 May 2024; Accepted: 9 July 2024; Available online: 11 July 2024

ABSTRACT: The direct conversion of methane into high-value chemicals has been a persistent research focus in the fields of chemical engineering and energy. Photocatalysis, as an innovative technology, not only circumvents the issues of catalyst sintering and carbon deposition associated with traditional thermal catalysis but also transcends thermodynamic limitations by providing new reaction pathways. Utilizing molecular oxygen as an oxidant generates various reactive oxygen species, offering unique thermodynamic advantages for methane conversion. This review summarizes the advancements in photocatalytic partial oxidation (PPOM) and oxidative coupling of methane (POCM) using oxygen as an oxidant. It discusses the activation mechanisms and reaction pathways of methane and oxygen in different systems, as well as the application of photochemical cycling strategies in methane conversion. Finally, it addresses the challenges in this field, proposes potential solutions, and offers perspectives on the future development of photocatalytic systems.

Keywords: Photocatalysis; Methane; Oxygen; Partial Oxidation; Oxidative Coupling; Photochemical looping

1. Introduction

As petroleum reserves continue to dwindle and environmental issues become increasingly severe, efforts are being made to expand and innovate within the traditional petrochemical industry while seeking new primary carbon sources to meet the demands of chemical production. Methane, which is abundant and cost-effective, is widely found in natural gas, coalbed methane, shale gas, and combustible ice, making it a promising alternative to the depleting petroleum resources [1–3]. However, as shown in Figure 1A, the methane molecule is a tetrahedral structure with a bond angle of 109.5°, exhibiting high symmetry and low polarizability. It is a typical non-polar molecule, with a C—H bond dissociation energy of 439 kJ·mol^{-1}. The molecular orbitals of methane reveal a very low energy for the highest occupied molecular orbital (HOMO) and a very high energy for the lowest unoccupied molecular orbital (LUMO), indicating that both donating and accepting an electron require substantial energy, making methane exceedingly difficult to activate [4]. Additionally, most methane reserves are located in remote areas, and the transportation and storage of gaseous methane are costly and prone to leakage, potentially causing significant environmental problems [5,6]. Therefore, converting methane into transportable and higher-value chemicals is a promising yet challenging approach [7].

Methane conversion can be categorized into two main types: direct and indirect conversion [8]. The indirect conversion of methane, also known as the syngas (H_2 and CO) route [9,10], involves reforming methane to syngas, which is then further converted into high-value chemical feedstocks such as ammonia, methanol, and olefins [11]. This is currently the primary commercial route for large-scale methane conversion [12–14]. However, indirect conversion methods such as dry reforming of methane (DRM) and steam reforming of methane (SRM) are thermodynamically unfavorable at room temperature (Table 1 and Figure 1B), requiring high temperatures and pressures, resulting in high energy consumption and costs, which are detrimental to sustainable development. Compared to these methane

https://doi.org/10.35534/prp.2024.10005

reforming reactions, partial oxidation of methane (POM) to syngas is a spontaneous reaction that can reduce energy consumption and produce a H_2/CO ratio of 2/1, which is more suitable for subsequent processes such as methanol synthesis and Fischer-Tropsch synthesis. Direct conversion of methane involves converting methane directly into high-value chemicals, such as liquid oxygenates and hydrocarbons [15,16]. Compared to indirect conversion, direct conversion bypasses intermediate steps, saving costs and utilizing methane more efficiently. Direct conversion of methane includes oxidative and non-oxidative pathways. The non-oxidative pathway, or non-oxidative coupling of methane (NOCM), is an endothermic reaction typically requiring extremely high temperatures (>1000 °C) to activate the inert C—H bond [17], which can easily cause catalyst deactivation due to carbon deposition [18]. Generally, introducing oxidants (e.g., O_2, H_2O_2) can effectively lower the Gibbs free energy of the reaction (Table 1 and Figure 1B), allowing the reaction to proceed under milder conditions. Oxidative pathways such as partial oxidation of methane (POM) and oxidative coupling of methane (OCM) are of particular interest due to their low energy consumption and good atom economy. Despite this, in industrial applications of thermal catalytic direct conversion of methane, it remains challenging to couple methane into C_{2+} hydrocarbons at very low temperatures and avoid the formation of a large amount of thermodynamically favored by-products such as CO_2 [19]. Partial oxidation of methane also struggles to selectively oxidize methane into oxygenates and typically requires expensive oxidants such as H_2O_2 [20].

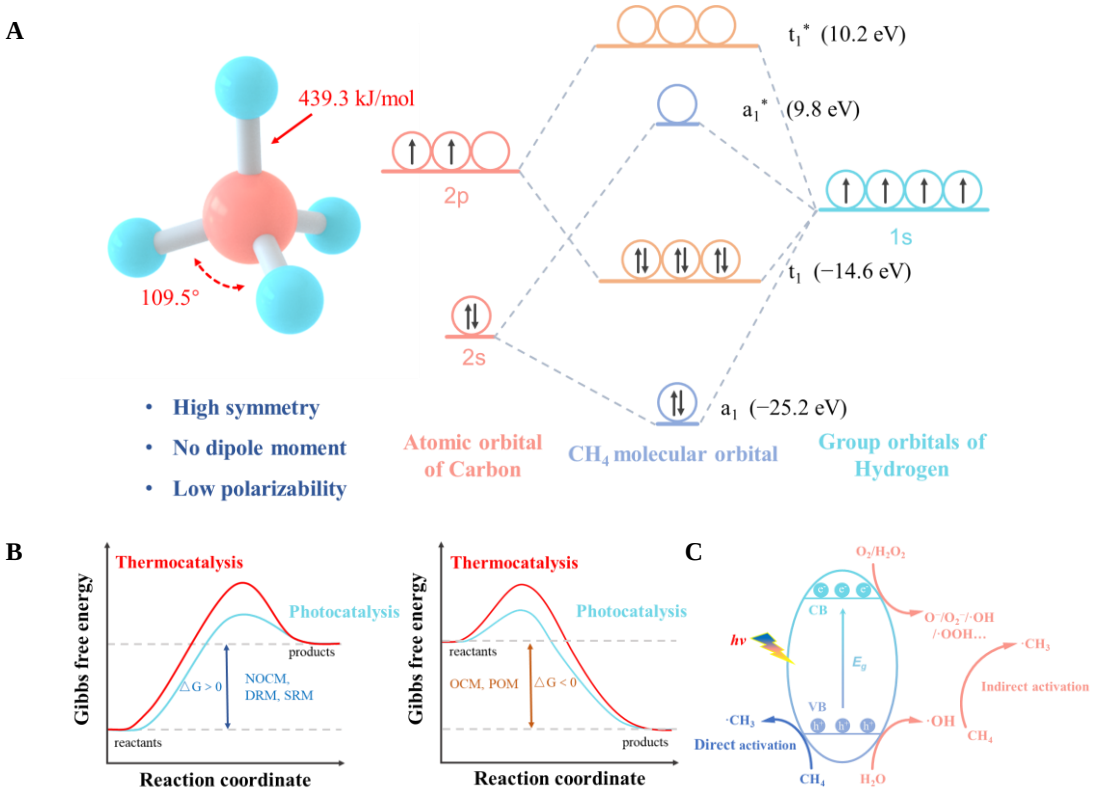

Figure 1. (**A**) Structure (left) and molecular orbital diagrams (right) of methane. * represents the antibonding orbitals. (**B**) Thermodynamically unfavourable (ΔG > 0) (left) and favourable (ΔG < 0) (right) reaction pathways for methane conversion operated at room temperature. (**C**) Schematic diagram of direct and indirect methane activation over a semiconductor photocatalyst.

Table 1. Change of Gibbs free energy for various methane conversion reactions.

Entry	Route	Reactions	Chemical Equations	ΔG^0 (298 K) kJ·mol^{-1}
1	Indirect	Steam reforming of methane (SRM)	$CH_4 + H_2O \rightarrow CO + 3H_2$	142
2		Dry reforming of methane (DRM)	$CH_4 + CO_2 \rightarrow 2CO + 2H_2$	171
3		Partial oxidation of methane (POM)	$2CH_4 + O_2 \rightarrow 2CO + 4H_2$	−173
	Direct	CH_4 and O_2		
4		Oxidative coupling of methane (OCM)	$2CH_4 + O_2 \rightarrow C_2H_4 + 2H_2O$	−287
5		Oxidative coupling of methane (OCM)	$4CH_4 + O_2 \rightarrow 2C_2H_6 + 2H_2O$	−320
6		Partial oxidation of methane (POM)	$2CH_4 + O_2 \rightarrow 2CH_3OH$	−223
7		Partial oxidation of methane (POM)	$2CH_4 + O_2 \rightarrow 2HCHO + 2H_2$	−104
		CH_4 and H_2O		
8		Partial oxidation of methane (POM)	$CH_4 + H_2O \rightarrow CH_3OH + H_2$	117
9		Partial oxidation of methane (POM)	$2CH_4 + H_2O \rightarrow C_2H_5OH + 2H_2$	162
		CH_4 only		
10		Non-oxidative coupling of methane (NOCM)	$2CH_4 \rightarrow C_2H_4 + 2H_2$	170
11		Non-oxidative coupling of methane (NOCM)	$2CH_4 \rightarrow C_2H_6 + H_2$	68.6

Photocatalysis, as an emerging technology, utilizes widely available and environmentally friendly solar energy to activate alkane's inert C—H bond under mild conditions [21–23]. As illustrated in Figure 1B, the introduction of photon energy significantly lowers the activation barrier for methane, breaking the thermodynamic equilibrium, which is crucial for achieving efficient low-temperature methane conversion [24–28]. Since the initial report by Kaliaguine et al. in 1978 on the photocatalytic conversion of methane, where CH_3O^- and $C_2H_5O^-$ species were observed on TiO_2 surfaces under UV irradiation [29], photocatalytic aerobic conversion of methane has garnered increasing attention. This process can be divided into two pathways: direct activation and indirect activation of methane [30]. As depicted in Figure 1C, when light irradiates the surface of a photocatalyst, photons with energy greater than the semiconductor band gap are absorbed, causing electrons to transition from the valence band (VB) to the conduction band (CB), leaving holes in the VB. The photogenerated electrons and holes migrate to the catalyst surface, where they can react with additional reactants such as H_2O, O_2, and H_2O_2 to generate reactive oxygen species (·OH, ·OOH, $\cdot O_2^-$), which assist in methane activation (indirect activation pathway). Photogenerated holes can also accumulate on lattice oxygen, forming O^-, thereby directly activating methane to generate $\cdot CH_3$ (direct activation pathway). Activated methane can then couple to form C_{2+} hydrocarbons (POCM) or combine with reactive oxygen species to form oxygenates (PPOM). Commonly used oxidants include H_2O_2, H_2O, and O_2. H_2O_2 is expensive, difficult to store and transport, and prone to decomposition under high pressure and heating, making it unsuitable for industrial applications. H_2O has low reactivity and is thermodynamically unfavorable (Table 1). In contrast, O_2 is economical, environmentally friendly, and thermodynamically favorable, providing unique advantages in photocatalytic aerobic conversion [31,32]. However, the complex nature of the reactive oxygen species generated by O_2 presents a significant challenge in controlling product selectivity for researchers.

This review summarizes recent advances in the photocatalytic conversion of methane using O_2 as the oxidant, focusing on the photocatalytic partial oxidation of methane (PPOM) and the oxidative coupling of methane (POCM). The reaction mechanisms in various systems, including C—H bond activation, O_2 reduction, and radical intermediate pathways, are examined, followed by an introduction to photochemical cycling strategies. Finally, the challenges and future prospects in the field of photocatalytic aerobic conversion of methane are discussed.

2. Photocatalytic Partial Oxidation of Methane (PPOM)

Total oxidation of methane produces low value CO_2, a greenhouse gas with adverse environmental impacts, making it unsustainable. In contrast, photocatalytic partial oxidation of methane (PPOM) can proceed under mild conditions to yield higher-value oxygenates (CO, CH_3OH, HCHO, CH_3CH_2OH, etc.). The choice of oxidant is crucial for the reactivity and selectivity of PPOM, and molecular oxygen, being inexpensive and environmentally friendly, is often used as the oxidant in the PPOM process. The coupling of O_2 reduction and CH_4 oxidation is thermodynamically favorable, and the reactive oxygen species (ROS) formed from O_2 reduction facilitate CH_4 activation and product formation.

Therefore, understanding the role of O_2 in the PPOM process is vital. Research in this area can be divided into gas-phase and liquid-phase systems.

2.1. Gas-Phase Systems

In gas-phase systems, methane can be photo-oxidized by O_2 to produce oxygenates such as CH_3OH, HCHO, and CO. In 1987, Brazdil's research team first achieved the photocatalytic conversion of CH_4 to CH_3OH on $CuMoO_4$ [33]. Under visible light irradiation and at 100 °C, using O_2 as the oxidant, a CH_3OH yield of 6 $\mu mol \cdot h^{-1}$ was achieved. The doping of Cu^{2+} extended the catalyst's visible light activity and prolonged the lifespan of O^-. Additionally, Shuben Li's research team achieved CH_4 photo-oxidation to CH_3OH at temperatures below 350 K and atmospheric pressure using Mo-doped porous TiO_2 catalysts pre-adsorbed with water [34]. In 2019, Xiaoyong Wu's research team reported a g-C_3N_4-modified $Cs_{0.33}WO_3$ photocatalyst (g-C_3N_4@$Cs_{0.33}WO_3$) that selectively photo-oxidized low-concentration CH_4 (1000 ppm) to CH_3OH at room temperature, with a yield of 4.38 $\mu mol \cdot g^{-1} \cdot h^{-1}$ [35]. As shown in Figure 2A, O_2 was activated to $\cdot O^{2-}$, which oxidized CH_4 on the g-C_3N_4 surface to methoxy radicals. Figure 2B illustrates two methoxy radical reaction pathways: in the selective oxidation pathway, photogenerated electrons from $Cs_{0.33}WO_3$ rapidly transfer to g-C_3N_4, preventing overoxidation of methoxy radicals, while the other pathway produces a small amount of CO_x, possibly due to overoxidation of CH_4 on g-C_3N_4 not bound to $Cs_{0.33}WO_3$. However, in gas-phase systems, product desorption is crucial, and the desorption of CH_3OH requires relatively high temperatures, which can lead to overoxidation. Therefore, producing liquid oxygenates (CH_3OH and HCHO) in gas-phase PPOM systems is challenging.

In contrast, gas-phase systems are more suitable for selective CO production. In 1988, Grätzel's research team achieved the photocatalytic conversion of CH_4 to CO at room temperature and atmospheric pressure using TiO_2-supported molybdenum oxide (TiO_2/MoO_3) [36]. Buxing Han's research team developed an Ag/AgCl@SiO_2 photocatalyst that selectively photo-oxidized CH_4 to CO, with a CO yield of 2.3 $\mu mol \cdot h^{-1}$ and a selectivity of 73% [37]. Mechanistic studies revealed that singlet $^1O_2$ generated in situ from O_2 could activate methane to form the key intermediate COOH*, which further dehydrates to form CO. Notably, this catalyst effectively photo-oxidized CH_4 to CO using sunlight in outdoor tests, demonstrating its practical application potential.

In the above works, the hydrogen products were H_2O. In contrast, converting CH_4 to hydrogen, especially syngas (CO and H_2), is more valuable and meaningful. In 2019, Miyauchi's research team proposed a PPOM scheme by loading Pd nanoparticles onto ultra-wide bandgap (UWBG) strontium tantalate ($Sr_2Ta_2O_7$) [38]. Compared to dark conditions, light irradiation reduced the starting temperature for syngas formation to below 423 K, and under external temperatures of 623 K and UV irradiation, CO and H_2 production rates reached 46.8 $mmol \cdot g^{-1} \cdot min^{-1}$ and 54.9 $mmol \cdot g^{-1} \cdot min^{-1}$, respectively. The photothermal carriers generated by interband excitation of Pd nanoparticles drove the photocatalytic reaction, with separated hot electrons and holes promoting the activation of O_2 and CH_4, respectively, while the thermal relaxation of carriers increased the catalyst surface temperature, further facilitating the reaction. The research team also incorporated a series of noble metals (Rh, Pd, Ru, and Pt) into MCM-41 molecular sieves, with Rh/MCM performing best, achieving efficient syngas production (CO selectivity ~50%) in a flow system at temperatures as low as 423 K, with a CH_4 quantum yield of 1.8% ($\lambda \geq 250$ nm) [39]. Similarly, the hot electrons and holes generated by interband excitation of metal nanoparticles directly activated adsorbed O_2 and CH_4, and the photothermal effect from carrier relaxation further promoted the reaction. Recently, Ordomsky's research team used conventional Cu(In,Ga)Se_2 (CIGS) absorbers to selectively photo-oxidize CH_4 to CO and H_2 at room temperature [40]. The CIGS films coated on Mo showed the best performance, with a CO yield of 2.4 $mmol \cdot g^{-1}$ and a CO/H_2 ratio of approximately 2:1, with CO selectivity exceeding 80%. As shown in Figure 2C, the reaction involves stepwise dissociation and coupling of CH_4 to form hydrocarbons, followed by dehydrogenation to form disordered carbon, and finally partial oxidation of carbon to CO. While photocatalytic partial oxidation of methane to CO and H_2 reduces reaction temperature and mitigates the explosion risk of premixed CH_4/O_2, the reaction still tends to produce more stable H_2O and CO_2, resulting in low selectivity for CO and H_2, and the CO/H_2 ratio is not 1:2, making it difficult to use directly for methanol or Fischer-Tropsch synthesis. Therefore, to apply photocatalytic partial oxidation of methane to syngas in industrial production, it is necessary to improve the selectivity and ratio of CO and H_2 and further reduce the reaction temperature.

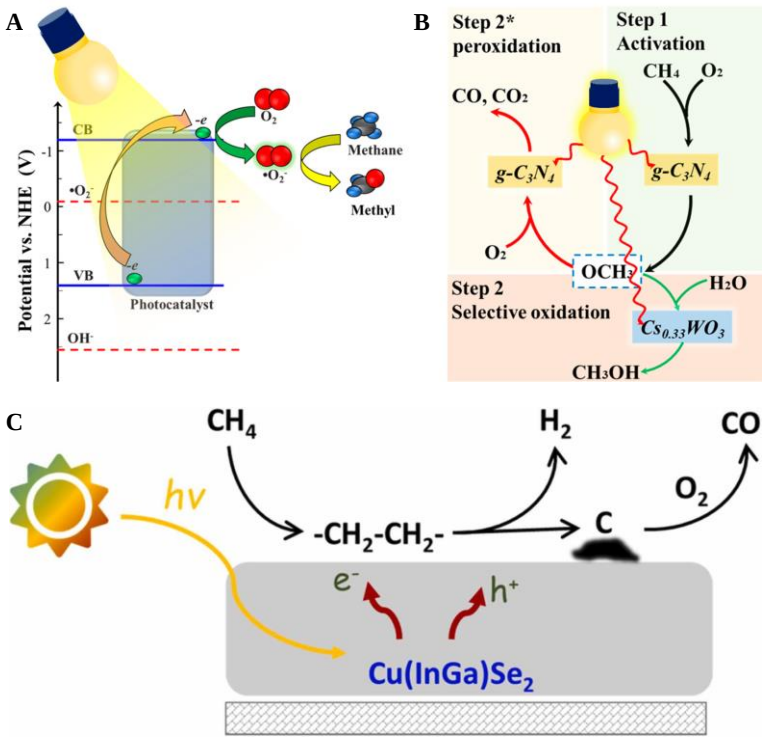

Figure 2. (**A**) Proposed O_2 activation mechanism and (**B**) Schematic illustration for PPOM over g-C_3N_4@$Cs_{0.33}WO_3$ [35]. (**C**) Schematic diagram of CH_4 partial oxidation to syngas over CIGS [40]. Note: Step 2 in Figure 2B represents selective oxidation and Step 2 * represents peroxidation.

2.2. Liquid-Phase Systems

Compared to gas-phase systems, using H_2O as a solvent in liquid-phase systems offers unique advantages. Firstly, H_2O can promote catalyst dispersion. Secondly, the presence of H_2O facilitates the desorption of liquid oxygenates from the catalyst surface, significantly inhibiting the overoxidation of liquid products and thus improving reaction selectivity. Additionally, the introduction of H_2O makes O_2 activation into reactive oxygen species (ROS) easier, while H_2O itself can also serve as a source of ROS. These ROS can promote the activation of CH_4 and the formation of products, although confirming the sources of ROS adds to the complexity of research. Based on the different ROS generated from O_2 activation, current research can be categorized into several types.

2.2.1. O_2 Activation to ·OOH

In 2019, JinHua Ye's research team first reported the use of O_2 as an oxidant to convert CH_4 into oxygenates in a liquid-phase system [41]. Under ambient conditions and light irradiation, different cocatalysts (Pt, Pd, Au, Ag) loaded on ZnO achieved efficient production of liquid oxygenates (CH_3OH and HCHO), with Au−ZnO showing the best performance, achieving a yield of 125 μmol·h^{-1} and a selectivity over 95%. Under light excitation, photogenerated holes and electrons on ZnO were separated, with CH_4 oxidized to ·CH_3 by photogenerated holes, while O_2, assisted by protonation in water, was reduced to ·OOH by photogenerated electrons on the cocatalyst. Subsequently, ·CH_3 and ·OOH combined to form the initial product CH_3OOH, which was further reduced to CH_3OH. HCHO could be produced by the photooxidation of CH_3OH by photogenerated holes or ·OH, or directly by the decomposition of CH_3OOH (Figure 3A). Isotope labeling experiments further confirmed that the O in CH_3OH originated from CH_3OOH, rather than from the coupling of ·CH_3 and ·OH generated from the photooxidation of water. Subsequently, the research team developed a dual-cocatalyst modified titanium dioxide photocatalyst (Au−CoO_x/TiO_2), achieving a primary product (CH_3OH and HCHO) yield of 2540 μmol·g^{-1}·h^{-1} and a selectivity of 95% under ambient conditions [42]. Mechanistic studies indicated that the excellent activity and selectivity stemmed from the synergistic effect of Au nanoparticles and CoO_x. Upon illumination, Au nanoparticles facilitated the separation of photogenerated carriers and the reduction of O_2, while ·OH generated from water oxidation could over-oxidize CH_3OH to HCHO and CO_2. CoO_x modulated the oxidative capacity of the photocatalyst, inhibiting the formation of highly oxidative ·OH, thus improving selectivity.

Junwang Tang's research team reported an Au−Cu alloy-modified ZnO ($Au_{0.2}Cu_{0.15}$−ZnO) achieving a primary product (CH_3OH, CH_3OOH, and HCHO) yield of 11,225 μmol·g^{-1}·h^{-1}, with nearly 100% selectivity and an apparent

quantum efficiency of 14.1% at 365 nm [43]. As shown in Figure 3B, Cu acted as the electron acceptor, reducing O_2 to ·OOH, while Au accepted photogenerated holes to oxidize H_2O to ·OH, synergistically promoting charge separation and methane conversion. Both ·OH and photogenerated holes could oxidize methane to $·CH_3$, and in ROS quenching experiments, the introduction of salicylic acid as a sacrificial agent for ·OH nearly halted methane conversion, proving that ·OH was the primary active species for methane activation. They also developed Pd–def–In_2O_3 [44], Pd–def–TiO_2 [45], Pd–def–WO_3 [46], and Cu–def–WO_3 [47] photocatalysts with similar PPOM mechanisms. Under light excitation, semiconductor supports generated photogenerated electron-hole pairs, with O_2 reduced to ·OOH radicals by photogenerated electrons and H_2O oxidized to ·OH by holes, further activating methane. These studies provide guidance for the rational design of future catalysts.

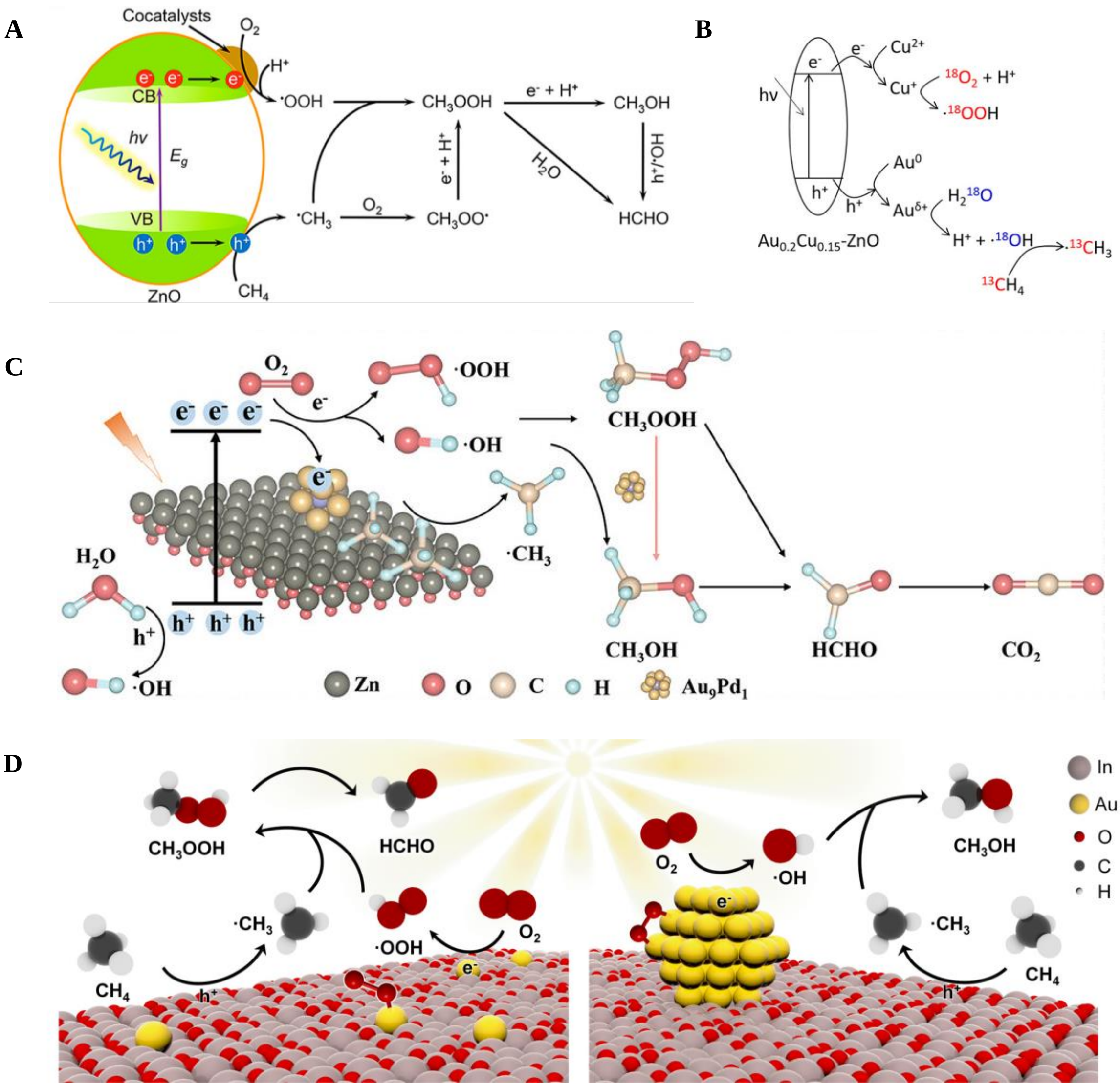

Figure 3. (**A**) Schematic diagram of photocatalytic CH_4 oxidation over cocatalyst/ZnO [41]. (**B**) Schematic illustration of photocatalytic methane conversion over $Au_{0.2}Cu_{0.15}$–ZnO [43]. (**C**) Proposed photocatalytic mechanism for the selective oxidation of CH_4 over Au_9Pd_1/ZnO with O_2 [48]. (**D**) Proposed mechanism for PPOM on Au_1/In_2O_3 (left) and Au_{NPs}/In_2O_3 (right) [49].

Jun Wang's research team reported AuPd nanoparticle-loaded defect ZnO nanosheets (Au_9Pd_1/ZnO) for efficient photocatalytic methane oxidation to oxygenates under ambient conditions, achieving a maximum liquid oxygenate yield of 152.2 $mM·g^{-1}·h^{-1}$ with a selectivity of 86.7% and an apparent quantum efficiency of 16.5% at 380 nm [48]. The excellent photocatalytic performance was attributed to the synergistic effect between the defect ZnO substrate and the AuPd cocatalyst. The former promoted CH_4 adsorption, while the latter enhanced light absorption, charge separation, and O_2 activation to ROS. As illustrated in Figure 3C, under illumination, electrons were excited from the valence band to the conduction band of ZnO, then transferred to Au_9Pd_1 nanoparticles, reducing O_2 to ·OOH and ·OH. Photogenerated holes remaining in the ZnO valence band could oxidize CH_4 to $·CH_3$ and H_2O to ·OH, although this process was less efficient. Thus, ROS generated from O_2 reduction played a dominant role in activating CH_4 adsorbed on ZnO

to $\cdot CH_3$. $\cdot CH_3$ could then interact with $\cdot OOH$ and $\cdot OH$ to form CH_3OOH and CH_3OH. In the presence of Au_9Pd_1 nanoparticles, CH_3OOH could be partially converted to CH_3OH via a two-electron reduction process, with further oxidation by holes or $\cdot OH$ leading to HCHO and CO_2 formation.

Zhiyong Tang's research team achieved selective generation of $\cdot OOH$ and $\cdot OH$ by adjusting the band structure and active site size of Au/In_2O_3, enabling efficient and selective production of HCHO and CH_3OH [49]. After three hours of photocatalytic CH_4 oxidation at room temperature, the HCHO yield on Au single-atom-loaded In_2O_3 (Au_1/In_2O_3) reached 6.09 $mmol \cdot g^{-1}$ with a selectivity of 97.62%, while Au nanoparticle-loaded In_2O_3 ($AuNPs/In_2O_3$) achieved a CH_3OH yield of 5.95 $mmol \cdot g^{-1}$ with a selectivity of 89.42%. Figure 3D summarizes the entire process of selective photocatalytic oxidation of CH_4 on Au/In_2O_3. For Au_1/In_2O_3, its valence band potential is more negative than the $H_2O/\cdot OH$ oxidation potential, preventing $\cdot OH$ generation during the reaction. Instead, photogenerated holes oxidize CH_4 to $\cdot CH_3$, while photogenerated electrons transferred to Au reduce adsorbed O_2, with end-on adsorbed O_2 favoring reduction to $\cdot OOH$. $\cdot OOH$ subsequently combines with $\cdot CH_3$ to form CH_3OOH, which decomposes to form HCHO. On the surface of Au nanoparticles, side-on adsorbed O_2 is more easily reduced to $\cdot OH$, which combines with $\cdot CH_3$ to form CH_3OH. This demonstrates that rational design of photocatalysts can precisely control the types of radicals formed.

2.2.2. O_2 Activation to $\cdot OH$

In liquid-phase PPOM systems, not only can H_2O be oxidized to produce $\cdot OH$, but O_2 can also be activated to $\cdot OH$, which participates in the reaction. The $\cdot OH$ radicals promote methane activation and product formation and participate in the oxidation of intermediates. However, an excess of $\cdot OH$ can lead to overoxidation of products, so controlling $\cdot OH$ formation is crucial for improving reaction activity and selectivity. In 2020, Zhiyong Tang's research team designed Au nanoparticle-modified ZnO photocatalysts that, for the first time, activated O_2 to $\cdot OH$ in a liquid-phase PPOM system [50]. Under ambient conditions and light irradiation, the Au/ZnO catalyst exhibited excellent performance, with a CH_3OH yield of 1371 $\mu mol \cdot g^{-1}$ and a selectivity of 99.1%. Isotope experiments with ^{18}O demonstrated that the O atoms in the product CH_3OH originated from both O_2 and H_2O, not just O_2. As shown in Figure 4A, Au nanoparticles act as electron conductors, effectively extracting electrons from the conduction band of ZnO and injecting them into O_2, producing $\cdot OH$ through the $O_2 \rightarrow H_2O_2 \rightarrow \cdot OH$ pathway. Simultaneously, holes remaining in the valence band of ZnO oxidize H_2O to $\cdot OH$. Subsequently, CH_4 is activated by the generated $\cdot OH$ to form $\cdot CH_3$, and finally, $\cdot OH$ and $\cdot CH_3$ directly combine to produce CH_3OH.

They also developed quantum-sized $BiVO_4$ ($q-BiVO_4$) capable of oxidizing methane to liquid oxygenates under visible light irradiation [51]. It was found that the selectivity for CH_3OH and HCHO could be regulated by altering the amounts of O_2 and H_2O in the reaction system, reaction time, and the wavelength and intensity of light irradiation. Shorter wavelengths and longer reaction times enhanced the oxidation ability towards CH_4, favoring HCHO formation under prolonged UV irradiation. Conversely, visible light irradiation and the introduction of large amounts of water to increase dissolved CH_4 content inhibited overoxidation, thereby increasing CH_3OH selectivity. In this system, O_2 is activated to $\cdot OH$, which activates CH_4 to form $\cdot CH_3$. $\cdot CH_3$ then combines with O_2, protons, and an electron to form CH_3OOH, which decomposes to produce CH_3OH, with further oxidation yielding HCHO (Figure 4B).

JinHua Ye's research team reported P-doped g-C_3N_4 (CNP) achieving a CH_3CH_2OH yield of 51 $\mu mol \cdot g^{-1} \cdot h^{-1}$ at 25 °C and 1 atm [52]. As shown in Figure 4C, P doping enhanced the process of O_2 activation through H_2O_2 ($O_2 \rightarrow H_2O_2 \rightarrow \cdot OH$) to generate $\cdot OH$, which activated CH_4 to form $\cdot CH_3$. $\cdot CH_3$ further formed CH_3CH_2OH along with small amounts of HCOOH and CO_2. Wenting Wu's research team constructed a sulfone-modified conjugated organic polymer that achieved photocatalytic conversion of CH_4 to CH_3OH and HCOOH under ambient light irradiation [53]. Mechanistic studies showed that light irradiation induced homolysis of S=O bonds on the catalyst, generating $\cdot O$ and $\cdot S$. $\cdot O$ could adsorb and activate CH_4, while $\cdot S$ provided electrons to $^1O_2$, generating H_2O_2, which then decomposed into $\cdot OH$, further oxidizing CH_4. Recently, the team also reported an Au−Pd alloy-modified ZnO photocatalyst ($Au-Pd_{0.5}/ZnO$) for CH_4 conversion to CH_3OH, achieving a CH_3OH yield and selectivity of 81.0 $\mu mol \cdot h^{-1}$ and 88.2%, respectively [54]. Unlike the traditional $O_2 \rightarrow H_2O_2 \rightarrow \cdot OH$ pathway, they proposed a strategy for efficiently generating $\cdot OH$ directly from $O_2 \rightarrow \cdot OOH \rightarrow \cdot OH$, improving CH_3OH yield and selectivity. As shown in Figure 4D, under light irradiation, photogenerated holes oxidize CH_4 to $\cdot CH_3$, while O_2 adsorbed on the Au−Pd alloy is reduced to $\cdot OOH$ by photogenerated electrons. The Au−Pd alloy facilitates O_2 adsorption and the cleavage of the O−O bond in $\cdot OOH$, quickly and directly converting $\cdot OOH$ to $\cdot OH$. Finally, $\cdot CH_3$ combines with $\cdot OH$ to form CH_3OH. This work not only provides a new strategy for efficiently generating $\cdot OH$ directly but also offers guidance for the precise design of composite photocatalysts for PPOM reactions.

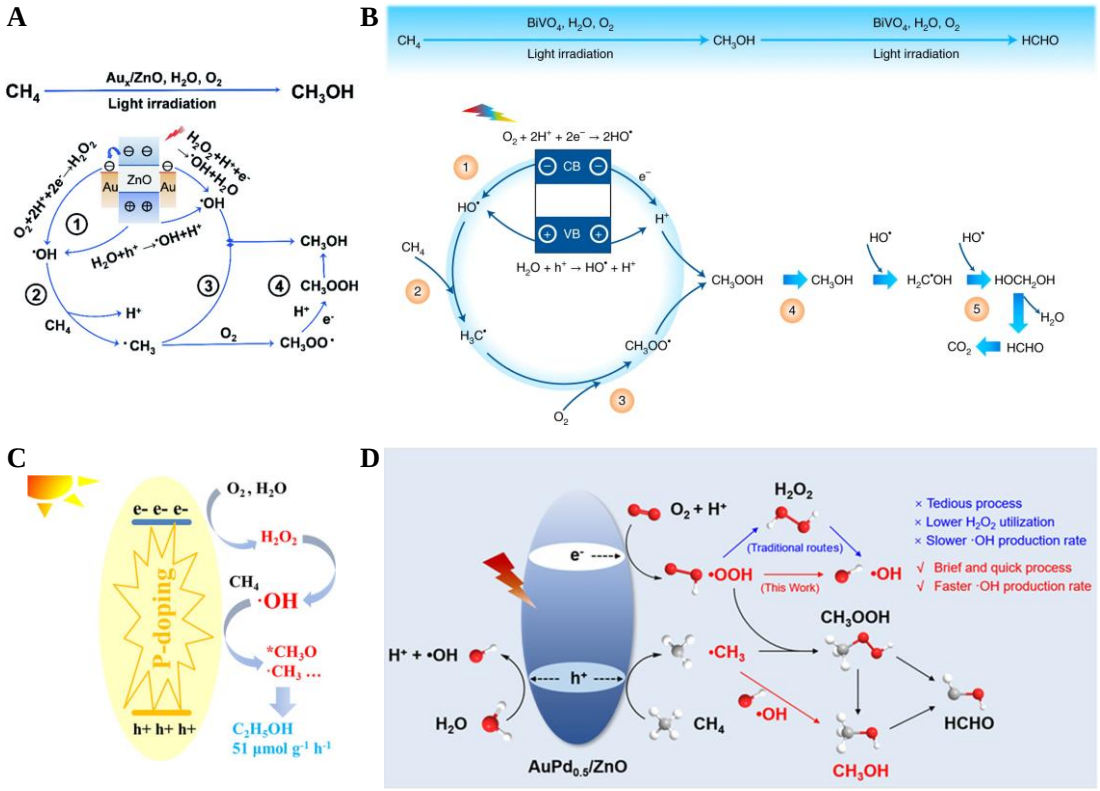

Figure 4. (**A**) Schematic illustration of photocatalytic CH_4 conversion on Au/ZnO [50]. (**B**) Proposed mechanism of photocatalytic CH_4 oxidation over q−$BiVO_4$ [51]. (**C**) Schematic diagram of photocatalytic methane conversion over CNP [52]. (**D**) Proposed mechanism of photocatalytic CH_4 oxidation on $AuPd_{0.5}$/ZnO [54].

2.2.3. O_2 Activation to $\cdot O_2^-$

O_2 can also be activated to $\cdot O_2^-$. Qin Kuang's research team developed a hollow porous Pd/H−TiO_2 photocatalyst, where the unique hollow structure and strong metal-support interaction synergistically promoted the photocatalytic conversion of CH_4 to CH_3OH [55]. As shown in Figure 5A, ·OH and $\cdot O_2^-$ are the primary active species involved in the photocatalytic process. Here, ·OH primarily activates methane to $\cdot CH_3$, while $\cdot O_2^-$ further converts $\cdot CH_3$ to CH_3OH.

Liangshu Zhong's research team reported a W-doped TiO_2 photocatalyst [56]. The W doping modified the electronic and band structure of TiO_2, achieving a yield of liquid oxygenates of 12.2 mmol·g^{-1} with a selectivity of 99.4%. Subsequently, they developed a Cu and W co-doped TiO_2 (Cu−W−TiO_2) photocatalyst, achieving an oxygenate yield of 34.5 mmol·g^{-1} with a selectivity of 97.1% [57]. Under light irradiation, O_2 was reduced to $\cdot O_2^-$ by photogenerated electrons or electrons captured in the W^{6+}/W^{5+} cycle, while CH_4 was activated to $\cdot CH_3$ by Cu^+. The $\cdot O_2^-$ combined with H^+ to form ·OOH, which reacted with $\cdot CH_3$ to form CH_3OOH, which was further reduced to CH_3OH. The synergistic effect of hole and electron capture processes on Cu−W−TiO_2 reduced the recombination of photogenerated carriers, promoting methane activation and efficient conversion. They also developed a $SrWO_4/TiO_2$ heterojunction catalyst [58]. The formation of the heterostructure facilitated the separation and transfer of photogenerated carriers, achieving an oxygenate yield of 13,365 μmol·g^{-1} and a selectivity of 98.7%. Yunhang Hu's research team reported an Au−Pd/TiO_2 photocatalyst, achieving a CH_3OH yield of 12.6 mmol·g^{-1}·h^{-1} in the presence of O_2 and H_2O [59]. As shown in Figure 5B, photogenerated electrons reduced O_2 to $\cdot O_2^-$, which was then converted to ·OOH. Meanwhile, H_2O was oxidized to ·OH by photogenerated holes, activating CH_4 to $\cdot CH_3$. $\cdot CH_3$ coupled with ·OOH to form CH_3OOH, which was further reduced to CH_3OH. TiO_2 absorbed UV light, generating electrons and holes, while Au−Pd nanoparticles not only facilitated the transfer of photogenerated electrons but also absorbed visible light, increasing the catalyst temperature. The increased temperature enhanced the process of H_2O oxidation to ·OH and drove the reduction of O_2 to $\cdot O_2^-$ and the conversion of CH_3OOH to CH_3OH. The synergistic effect of Au−Pd nanoparticles and TiO_2 facilitated the efficient conversion of CH_4 to CH_3OH.

Li Niu's research team prepared Au nanoparticle-modified cubic WO_3 (c−WO_3) for the selective photo-oxidation of CH_4 to HCHO [60]. $^{18}O_2$ isotope tests indicated that the O in HCHO originated from lattice oxygen on the exposed (002), (020), and (200) planes of c−WO_3, and the surface-consumed lattice oxygen could be regenerated by the reduction

of O_2. Under light irradiation, W^{5+} and O^- were generated on the c−WO_3 surface. O^- cleaved the C—H bond, activating CH_4 to $-OCH_3$, which was further dehydrogenated by adjacent terminal O^- to form $HOCH_2OH$, and finally dehydrated to form HCHO. Au nanoparticles captured photogenerated electrons, further facilitating the formation of O^-. JinHua Ye's research team achieved a CH_3OH yield of 4.8 mmol·g^{-1}·h^{-1} with a selectivity of about 80% using Ag-modified TiO_2 with a dominant (001) facet to inhibit PPOM overoxidation [61]. As shown in Figure 5C, on the TiO_2(001) surface, photogenerated holes oxidized surface oxygen to form oxygen vacancies. O_2 reduced by photogenerated electrons formed $\cdot O_2^-$, which were stabilized by oxygen vacancies, forming surface superoxides (Ti−$O_2^{\cdot}$). These could capture photogenerated electrons, forming surface peroxides (Ti−OO−Ti and Ti−(OO)), which dissociated into Ti−$O^{\cdot}$ pairs. These pairs could directly activate CH_4 to form CH_3OH, effectively avoiding the formation of $\cdot CH_3$ and ·OH, thus inhibiting overoxidation.

Zhiyong Tang's research team used a "pause-flow" reactor with a TiO_2 dual-phase catalyst (anatase 90% and rutile 10%) (anatase/rutile) for the highly selective conversion of CH_4 to HCHO, achieving an HCHO yield of 8.09 mmol·g^{-1}·h^{-1} with a selectivity of 97.4% [62]. Under light irradiation, carriers were generated inside A/R−TiO_2, with O_2 activated to $\cdot O_2^-$ on R−TiO_2. The $\cdot O_2^-$ was further activated to O^- species, activating CH_4 to $*CH_3O$. $*CH_3O$ was converted to CH_3OH, desorbed with the assistance of H_2O, and finally oxidized to HCHO by ·OH. The O^- species originated from TiO_2 lattice oxygen, with O_2 filling the oxygen vacancies in TiO_2 (Figure 5D). This work guides the rational design of catalysts and reactors for industrial photocatalytic conversion of low-carbon feedstocks and demonstrates the feasibility of large-scale formaldehyde production.

In the PPOM process, controlling the selectivity for single oxygenate products remains a significant challenge. O_2 activation can produce various ROS, each with different oxidation capabilities and mechanisms for activating CH_4. Future research should focus on the rational design of photocatalysts to precisely control the type of ROS generated, thereby controlling intermediate formation to enhance reaction efficiency and selectivity. Additionally, current photocatalytic methane partial oxidation reactions primarily occur in closed systems. While some progress has been made, the limitations of closed systems restrict large-scale production of oxygenates. Therefore, future research should focus on developing reaction systems and designing reactors to achieve efficient methane conversion on a larger scale, paving the way for industrial photocatalytic methane conversion.

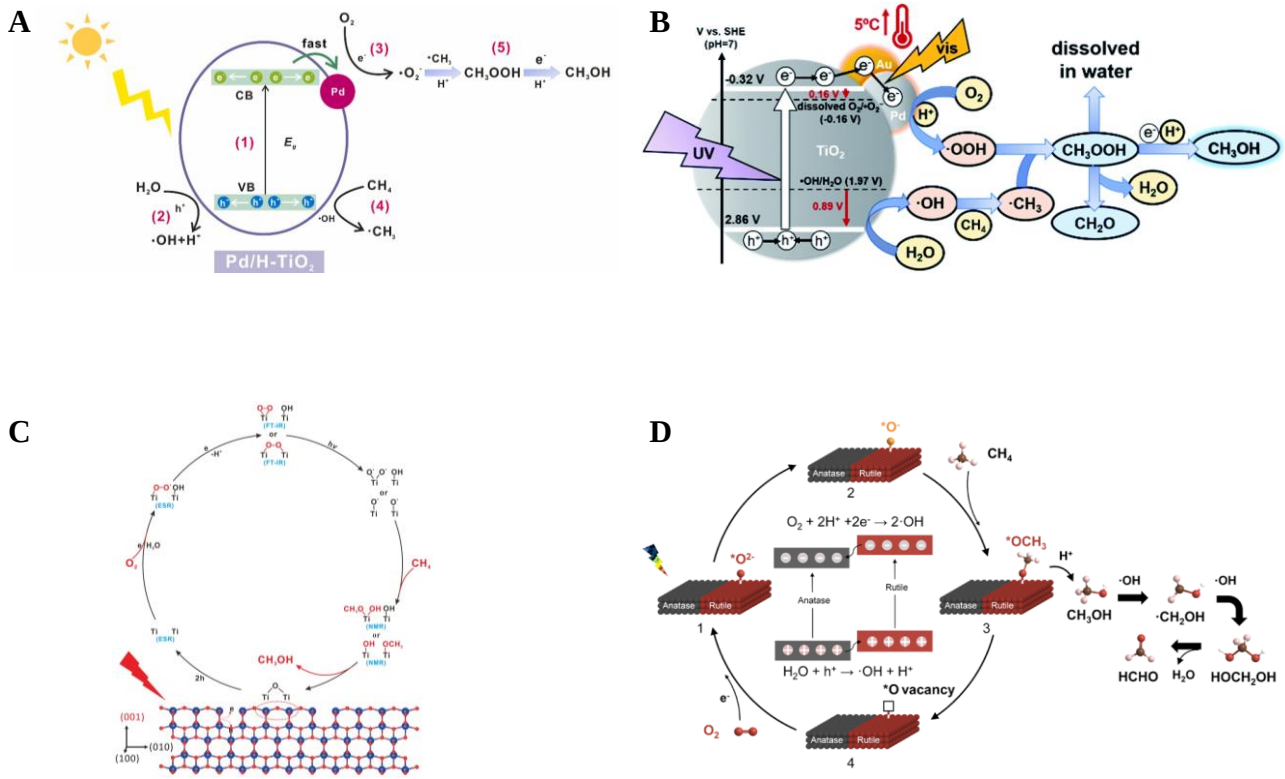

Figure 5. (**A**) Schematic illustration for the oxidation of methane to methanol over Pd/H−TiO_2 [55]. (**B**) Schematic diagram of photocatalytic methane conversion over Au–Pd/TiO_2 [59]. (**C**) Proposed mechanism for CH_4 oxidation by O_2 on the (001) facets of TiO_2 [61]. (**D**) Proposed mechanism of photocatalytic methane oxidation on A/R−TiO_2 [62].

3. Photocatalytic Oxidative Coupling of Methane (POCM)

The oxidative coupling of methane (OCM) refers to the conversion of methane into C_{2+} hydrocarbons in the presence of an oxidant (typically O_2) [63]. Since Keller and Bhasin first reported the OCM production of valuable chemicals like ethylene and ethane in 1982 [64], the OCM reaction has garnered increasing attention. However, while the introduction of O_2 lowers the Gibbs free energy of the reaction, it still requires relatively high reaction temperatures and inevitably generates overoxidized products such as CO and CO_2. Therefore, photocatalytic oxidative coupling of methane (POCM) under mild conditions has become a new research hotspot. Researchers have deeply studied catalyst design, reactor optimization, and reaction mechanisms, achieving some significant results (Table 2).

Table 2. Representative works on photocatalytic OCM reaction with O_2 as the oxidant.

Catalyst	Reaction Condition	C_2 Yield Rate ($\mu mol \cdot g^{-1} \cdot h^{-1}$)	C_2 Selectivity	Stability	Ref.
Au/m−ZnO−4.8	Batch reactor, CH_4/O_2 = 2.5:1, 1 mg catalyst, room temperature, 300 W Xe lamp	19.5	–	–	[65]
Au/ZnO	Batch reactor, CH_4/O_2 = 99/1, 5 mg catalyst, 354.3 K, 365 nm LED	577	65%	12 cycles, 4 h on a cycle	[66]
ZnO	Batch reactor, CH_4/O_2 = 5/1, 50 mg catalyst, 298 K, 300 W Xe lamp	787.3	93%	–	[67]
$Au/ZnGa_2O_4$	Batch reactor, CH_4/O_2 = 2.5/1, 10 mg catalyst, room temperature, 300 W Xe lamp	1315.3	53%	5 cycles, 4 h on a cycle	[68]
$Au_{2.6\%}/Bi_2WO_6$	Batch reactor, CH_4/O_2 = 17/3, 20 mg catalyst, 403 K, 100W 365 nm LED	1690	85%	3 cycles, 3 h on a cycle	[69]
$Au/TiO_2{-}NV_o$	Batch reactor, CH_4/O_2 = 37.5/1, 10 mg catalyst, 393 K, 300 W Xe lamp	2872	80%	12 cycles, 1 h on a cycle	[70]
Au/ZnAl−v	Batch reactor, CH_4/O_2 = 160/0.3, 10 mg catalyst, 313 K, 300 W Xe lamp Flow reactor, CH_4/air = 99/1, 5 mg catalyst, 313 K, 300 W Xe lamp	81.6 (batch reactor) 3912 (flow reactor)	90.3% (batch reactor) 92% (flow reactor)	100 h in a flow reactor	[71]
$Cu_{0.1}Pt_{0.5}$/PC−50	Flow reactor, CH_4/O_2 = 400/1, 100 mg catalyst, 313 K, 40 W 365 nm LED	68	60%	8 h	[72]
$Pd_{1.8}{-}TiO_2$	Flow reactor, CH_4/O_2 = 90/1, 50 mg catalyst, room temperature, 365 nm LED	818	80.4%	–	[73]
$PdCu/TiO_2$	Flow reactor, CH_4/O_2 = 373/1 or 53/1, 50 mg catalyst, 303 K, 40 W 365 nm LED	950 (CH_4/O_2 = 373/1) 1240 (CH_4/O_2 = 53/1)	75% (CH_4/O_2 = 373/1) 52% (CH_4/O_2 = 53/1)	112 h (CH_4/O_2 = 373/1)	[74]
$Ag{-}AgBr/TiO_2$	Flow reactor, CH_4/air/Ar = 40/1/360, 6 bar, 100 mg catalyst, 313 K, 365 nm LED	354	79%	12 h	[75]
$Au{-}ZnO/TiO_2$ (4/1)	Flow reactor, CH_4/air = 69/1, 20 mg catalyst, 413 K, 300 W Xe lamp	5000	90%	12 h	[76]
$14{-}nm{-}Au/TiO_2$	Flow reactor, CH_4/O_2 = 40/1, 20 mg catalyst, 348 K, 400 W Hg-Xe lamp	819	86%	8 h	[77]
$Au60s/TiO_2$	Flow reactor, CH_4/O_2 = 133/1, 20 mg catalyst, 393 K, 100 W 365 nm LED	23,950	86%	30 h	[78]
$Au_{2.0\%}/TiO_2$	Flow reactor, CH_4/O_2 = 24/1, 5 mg catalyst, 427 K, 300 W Xe lamp	18,800	87%	240 h	[79]

3.1. Batch Systems

In 2018, Jinlin Long's research team achieved room-temperature photocatalytic coupling of methane to ethane using Au nanoparticles supported on porous ZnO nanosheets (Au/m−ZnO−4.8) [65]. The plasmonic field formed at the Au/ZnO interface effectively induced charge separation in photo-excited ZnO, initiating methane activation at the Zn sites. Mechanistic studies revealed that the rate-determining step for methane coupling was the reduction of protons by hot electrons induced by Au plasmonics. The introduction of O_2 generated reactive oxygen species (ROS), accelerating proton consumption and increasing the ethane production rate from 11.0 μmol·g^{-1}·h^{-1} to 19.5 μmol·g^{-1}·h^{-1}. Tierui Zhang's research team systematically elucidated the photocatalytic OCM mechanism by designing a series of transition metal (Au, Ag, Pd, Cu, Ni, Ru, and Pt)-supported ZnO nanoparticles (M/ZnO) [66]. They found that whether *CH_3 underwent C—C coupling or deep dehydrogenation on the metal surface was closely related to the d−σ interaction between *CH_3 and the metal. Au/ZnO achieved the highest C_2−C_4 yield of 683 μmol·g^{-1}·h^{-1} (selectivity 83%) due to strong d-σ hybridization between *CH_3 and Au, which reduced the Au—C—H bond angle, decreasing the spatial hindrance for *CH_3 coupling along the C—C pathway. As shown in Figure 6A, photoexcited Zn^+−O^- active sites on ZnO efficiently activated methane to *CH_3 and adsorbed H_2O, followed by selective coupling of *CH_3 on the metal surface to form ethane or overoxidation to CO_2. Meanwhile, O_2 was reduced by photogenerated electrons, following the pathway $O_2 \rightarrow O_2^- \rightarrow O_2^{2-} \rightarrow 2O^- \rightarrow 2O^{2-}$, replenishing the O_v created by H_2O desorption on ZnO. Scholten's research team synthesized ZnO nanostructures with photocatalytic OCM activity using the hydrolysis of imidazole zinc chloride ionic liquids (ILs). The size and shape (irregular particles, nanorods) of the ZnO nanostructures depended on the synthesis conditions [67]. When the ionic liquid to $ZnCl_2$ ratio was equimolar, the resulting irregular ZnO particles had the highest C_2H_6 yield (787.3 μmol·g^{-1}·h^{-1}) and a selectivity of about 93%. This result provides a new approach to designing efficient POCM catalysts under room temperature and non-metal conditions.

In addition to using classic ZnO semiconductors as POCM supports, researchers have explored other high-activity supports, achieving some progress. In 2023, Li Li's research team used Au nanoparticle-modified $ZnGa_2O_4$ nanosheets (Au/$ZnGa_2O_4$) for the photocatalytic oxidative coupling of methane, achieving an ethane yield of 1315.3 μmol·g^{-1}·h^{-1} and a selectivity of 53% [68]. The results showed that the reaction activity significantly increased compared to pure $ZnGa_2O_4$ due to Au nanoparticles promoting O_2 adsorption and activation, producing O_2^-. O_2^- was further reduced by photogenerated electrons to O^-, which cracked CH_4 to ·CH_3. Au nanoparticles effectively stabilized ·CH_3 and prevented its overoxidation to CO_2. Similarly, Dunwei Wang's research team achieved an ethane yield of 1690 μmol·g^{-1}·h^{-1} and a selectivity of 85% by constructing an $Au_{2.6\%}/Bi_2WO_6$ model to regulate ROS [69]. The study found that OCM performance was highly sensitive to the properties of the photocatalyst, which should facilitate the release of surface lattice oxygen, forming oxygen vacancies more easily. Au cocatalysts enhanced lattice oxygen activity, promoting O_v formation. Bi_2WO_6 has tunable surface oxygen, and under light irradiation, lattice oxygen was excited, activating the C—H bond in CH_4. The resulting ·CH_3 migrated to Au sites, where another CH_4 molecule was activated, producing a desorbable H_2O molecule and leaving an O_v. O_2 filled the O_v (Figure 6B). Throughout the process, O^{2-} was the active species, so ·CH_3 was more likely to couple at Au sites to form C_2H_6 rather than over-oxidize to CO_2.

Zizhong Zhang's research team achieved high activity and selectivity for photocatalytic OCM by constructing dual-active sites (N and oxygen vacancies) on TiO_2 nanosheets, regulating O_2 activation pathways [70]. Due to the different O_2 activation sites on TiO_2, the alkane yield on TiO_2 nanosheets with N and O_v dual-active sites (Au/TiO_2−NV_o) increased from 1600 μmol·g^{-1}·h^{-1} to 3200 μmol·g^{-1}·h^{-1}, and the selectivity improved from 61% to 93% compared to regular Au/TiO_2 nanosheets. For Au/TiO_2, O_2 easily captured photogenerated electrons on TiO_2, forming O_2^-, which tended to react with ·CH_3 intermediates to form $^-OOCH_3$, which further decomposed into H_2O and CO_2, leading to CH_4 overoxidation. For Au/TiO_2−NVo, as shown in Figure 6C, O_2 adsorbed on oxygen vacancies was reduced to O_2^-, and under the action of excited N atoms, the O−O bond of O_2^- cleaved, forming milder $O^{\cdot-}$ active species. $O^{\cdot-}$ could cleave the C—H bond in CH_4 to form ·CH_3, and hydroxyl radicals formed by the photolysis of Ti−O bonds activated the second CH_4. ·CH_3 coupled on Au NPs to form C_2H_6. After O atoms refilled the oxygen vacancies, the process continued with another two CH_4 molecules, inhibiting CH_4 overoxidation and enhancing OCM activity and selectivity. Unlike traditional oxide catalysts for POCM reactions, Yufei Song's research team achieved an ethane yield of 81.6 μmol·g^{-1}·h^{-1} and a selectivity of 90.3% by constructing Au-loaded ZnAl layered double hydroxide with oxygen vacancies (Au/ZnAl-v) [71]. In a batch system, the catalytic activity was stable for 100 h in a flow system, with a CH_4 conversion rate of 8.5 mmol·g^{-1}·h^{-1} and a C_2H_6 selectivity of 92%. The study found that introducing O_v into ZnAl-LDH significantly promoted the efficiency and selectivity of photocatalytic OCM. O_2 first adsorbed and activated on Ov, then the activated O_2 cleaved the C—H bond in CH_4. The resulting ·CH_3 migrated to Au sites, coupling to form ethane.

This report provides a new approach to designing efficient, selective, and stable photocatalytic materials for OCM using non-traditional oxide supports.

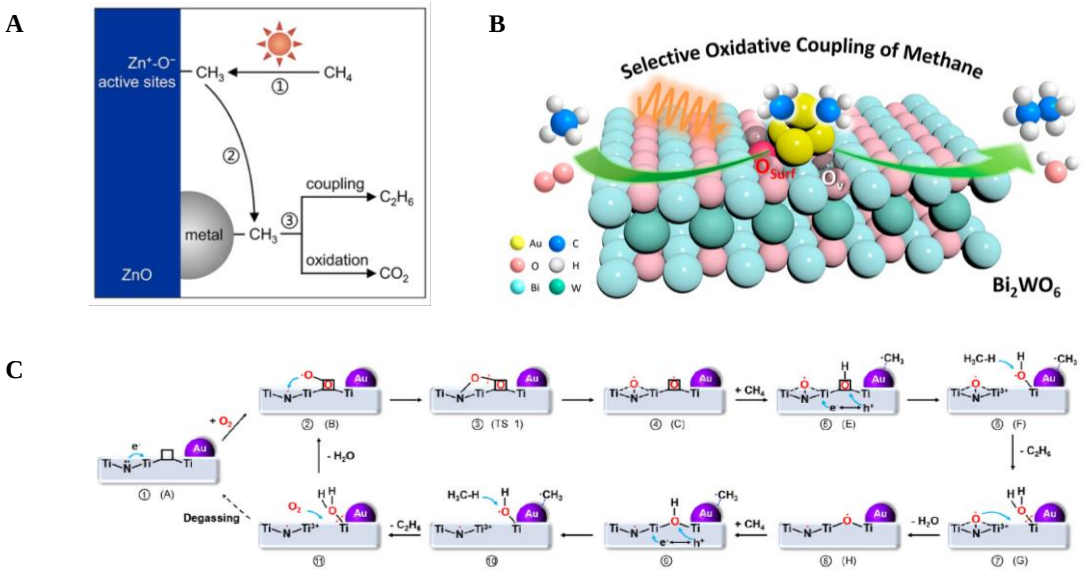

Figure 6. (**A**) Schematic diagram of the proposed reaction mechanism for photocatalytic OCM on metal/ZnO [66]. (**B**) Schematic description of Au-modified Bi_2WO_6 nanosheets for POCM [69]. (**C**) Proposed reaction mechanism of the POCM on Au/TiO_2–NV_o [70].

3.2. Flow Systems

In batch systems, although gas-catalyst contact is sufficient, prolonged residence time inevitably leads to overoxidation of CH_4, resulting in lower selectivity. Additionally, scaling up batch reactors to industrial production is challenging. Therefore, developing flow reaction systems is essential for achieving efficient and selective photocatalytic OCM.

In 2020, Junwang Tang's research team first reported photocatalytic OCM in a flow reaction system [72]. They introduced Pt nanoparticles and CuO_x clusters onto TiO_2 (PC-50) ($Cu_{0.1}Pt_{0.5}$/PC-50), achieving a C_2 hydrocarbon yield of 68 μmol·g^{-1}·h^{-1} and a selectivity of 60% under ambient conditions. The synergistic effect of Pt nanoparticles and CuO_x clusters increased the C_2 hydrocarbon yield by 3.5 times compared to PC-50 and more than twice the combined activity of Pt/PC-50 and Cu/PC-50. Under light irradiation, electrons were excited from the valence band to the conduction band of TiO_2 and migrated to Pt, while photogenerated holes transferred to CuO_x clusters. This process delayed carrier recombination and lowered the oxidation potential of photogenerated holes, preventing overoxidation of CH_4. CH_4 was activated by photogenerated holes on CuO_x clusters, forming ·CH_3 and H^+, with ·CH_3 coupling to form C_2H_6. Pt nanoparticles reduced O_2 and combined H^+ to remove it as H_2O.

Similarly, the research team used Pd nanoparticle-modified anatase TiO_2 ($Pd_{1.8}$–TiO_2) to achieve a C_2H_6 yield of 818 μmol·g^{-1}·h^{-1} under mild conditions, which was 13 times that of pure TiO_2, with a selectivity of 80.4% [73]. Pd nanoparticles acted as photogenerated hole acceptors, participating in CH_4 activation and ·CH_3 coupling, effectively inhibiting photogenerated carrier recombination, thereby significantly improving catalyst performance. They further reported a highly efficient and stable PdCu nanoalloy-modified TiO_2 (PdCu/TiO_2) photocatalyst for OCM in a mild flow system, achieving a C_2 hydrocarbon yield of 1240 μmol·g^{-1}·h^{-1} and the photocatalyst exhibits the turnover frequency and turnover number of 116 h^{-1} and 12,642 with respect to PdCu. [74]. As shown in Figure 7A, under light irradiation, photogenerated electrons from TiO_2 reduced O_2 to superoxide radicals, while photogenerated holes transferred to the PdCu alloy to activate adsorbed CH_4, generating ·CH_3 and H^+. ·CH_3 further coupled to form C_2H_6, with H^+ consumed by superoxide radicals to form H_2O. Introducing Pd nanoparticles into TiO_2 led to effective charge transfer, weakening the C—H bond in CH_4 and facilitating its activation, producing more ·CH_3. Cu reduced the adsorption energy of the target product C_2H_6, preventing catalyst coking. Thus, the synergistic effect of PdCu nanoalloy achieved efficient, selective, and stable photocatalytic OCM. Additionally, they designed an Ag–AgBr/TiO_2 ternary catalyst and studied the effect of reaction pressure on photocatalytic OCM performance in a pressurized flow reactor [75]. When the reaction pressure increased from 1 bar to 6 bar, the C_2H_6 yield increased from 18.2 μmol·g^{-1}·h^{-1} to 354 μmol·g^{-1}·h^{-1}, with a C_{2+} selectivity of 79%. Higher reaction pressure enhanced the mass transfer efficiency of reactants and products, improving reaction efficiency and selectivity. Ag nanoparticles, as electron acceptors, facilitated charge transfer, while

the AgBr and TiO_2 heterostructure reduced oxidation capability, preventing overoxidation. Thus, designing high-performance catalysts and rational reaction systems is crucial for photocatalytic OCM.

Au NPs, as a cocatalyst, not only promote charge separation but also stabilize $\cdot CH_3$, preventing CH_4 overoxidation to CO_2, thereby improving photocatalytic OCM activity and selectivity. Moreover, the electromagnetic decay of localized surface plasmon resonance (LSPR) on Au nanoparticles can generate hot carriers. Hot carrier relaxation can induce a photothermal effect and the hot carrier separation not only promotes O_2 reduction and CH_4 activation, but also prolongs carrier lifetime. Therefore, using Au NPs as cocatalysts in photocatalytic OCM is favored by researchers. In 2021, JinHua Ye's research team efficiently and selectively coupled CH_4 to C_2H_6 using Au NP-loaded ZnO/TiO_2 hybrids ($Au{-}ZnO/TiO_2(4/1)$), achieving a C_2H_6 yield of over 5000 $\mu mol \cdot g^{-1} \cdot h^{-1}$ with 90% selectivity [76]. The study found that modifying ZnO with TiO_2 and Au formed a $ZnO/TiO_2{-}Au$ heterojunction, enhancing photocatalytic activity while maintaining ZnO's mild C—H bond overoxidation capability in CH_4. Introducing Au cocatalysts promoted O_2 adsorption and activation, facilitating the desorption of $*CH_3$ as $\cdot CH_3$ in the gas phase, thus promoting C_2H_6 formation and inhibiting overoxidation to CO_2. As shown in Figure 7B, under light irradiation, the photocatalyst generated photogenerated electrons and holes, with the heterojunction allowing rapid electron transfer to Au NPs, reducing O_2 to $*O_2^-$, while photogenerated holes transferred to ZnO, aiding CH_4 activation to produce $*CH_3$. $*CH_3$ desorbed as $\cdot CH_3$ on Au and coupled to form C_2H_6. C_2H_6 further reacted with holes to form $\cdot C_2H_5$, which coupled with $\cdot CH_3$ to form C_3H_8 or further oxidized to C_2H_4, with H_2O as a byproduct. Unlike Au, Pt, with stronger O_2 reduction capability, tended to form $*OCH_3$, ultimately oxidizing to CO_2. A lower O_2/CH_4 ratio meant less collision between *O and $*CH_3$, inhibiting CH_4 overoxidation. Therefore, the O_2/CH_4 ratio in feed gas significantly controls product selectivity.

Subsequently, Khodakov's research team studied the role of 6–60 nm plasmonic Au NPs supported on TiO_2 in methane oxidative coupling. Under optimized conditions with 14 nm Au NPs ($14{-}nm{-}Au/TiO_2$), an ethane yield of 819 $\mu mol \cdot g^{-1} \cdot h^{-1}$ and a selectivity of 86% were achieved [77]. They found that the size (6–60 nm) and amount (>0.5 wt%) of Au NPs did not significantly affect methane coupling. Under UV excitation, TiO_2 generated oxygen vacancies, activating methane at these sites, while Au NPs activated O_2 and facilitated charge separation. Using a rapid sputtering method, Junwang Tang's research team synthesized highly efficient $Au60s/TiO_2$ catalysts on glass fiber filters, achieving a C_2 hydrocarbon yield of 23,950 $\mu mol \cdot g^{-1} \cdot h^{-1}$ with 86% selectivity, the highest reported efficiency to date [78]. Introducing Au NPs as cocatalysts extended the lifetime of TiO_2 photoelectrons by 66 times, forming more superoxide radicals, promoting the photocatalytic methane conversion cycle. As catalytic centers and photogenerated hole acceptors, Au NPs facilitated methane adsorption and increased photogenerated hole numbers, favoring selective C—H bond cleavage and C—C bond coupling. Under light irradiation, TiO_2 generated photogenerated electrons and holes, with photogenerated holes transferring to Au NPs while long-lived photogenerated electrons on TiO_2 reduced oxygen. Au efficiently adsorbed and activated CH_4, generating $\cdot CH_3$ and H^+, with $\cdot CH_3$ coupling to form C_2H_6 and H^+ combining with superoxide radicals to form H_2O (Figure 7C).

Recently, Yujie Xiong's research team loaded Au NPs onto TiO_2 nanosheets ($Au_{2.0\%}/TiO_2$), achieving a C_{2+} hydrocarbon yield of 19,280 $\mu mol \cdot g^{-1} \cdot h^{-1}$ with 90% selectivity in a custom 3D-printed multi-point injection flow reactor, maintaining stability for over 240 h [79]. Unlike pure TiO_2, where O_2^- induced CH_4 overoxidation, the presence of Au NPs stabilized $*CH_3$ intermediates and constructed an $Au{-}TiO_2$ interface, regulating O_2 activation to produce mild O_2^{2-} species, avoiding $*CH_3$ overoxidation. The localized electric field induced by Au NPs' LSPR promoted the polarization and dissociation of C—H bonds in CH_4. As shown in Figure 7D, under light irradiation, photogenerated electrons in the TiO_2 conduction band were captured by Au NPs, achieving O_2 activation at the $Au{-}TiO_2$ interface, generating mild O_2^{2-} species. These mild O_2^{2-} species dissociated adsorbed CH_4 on Au NPs to produce $*CH_3$. Another CH_4 underwent a similar process to generate $*CH_3$, which coupled to form C_2H_6. The two formed *OH radicals continued to abstract hydrogen atoms from two other CH_4 molecules, generating a second C_2H_6 and two H_2O molecules, regenerating O_2 activation sites, completing the photocatalytic OCM cycle. This work guides the synergistic design of reactors and photocatalysts to simultaneously regulate mass transfer and reactant activation for high-performance flow systems.

In summary, future research should focus on reaction system and photocatalyst design. For reaction systems, flow systems have improved reaction efficiency and target product selectivity, but issues such as low mass transfer efficiency and product separation remain. Designing more efficient reactors to control the catalytic conversion process is necessary. Additionally, the CH_4/O_2 ratio, flow rate, and reaction pressure significantly impact photocatalytic OCM performance. Therefore, ensuring safety requires finer control of reaction conditions. For photocatalyst design, rational catalysts should generate mild active oxygen species to promote methane activation while stabilizing methyl intermediates to facilitate C—C bond coupling. Currently, most cocatalysts are Au or other precious metals, and the main product is ethane, which has lower commercial value. Considering economic feasibility, developing non-precious metal catalysts

and novel catalysts to regulate CH_4 activation and carbon intermediate conversion to produce higher-value chemicals such as ethylene and propane is essential.

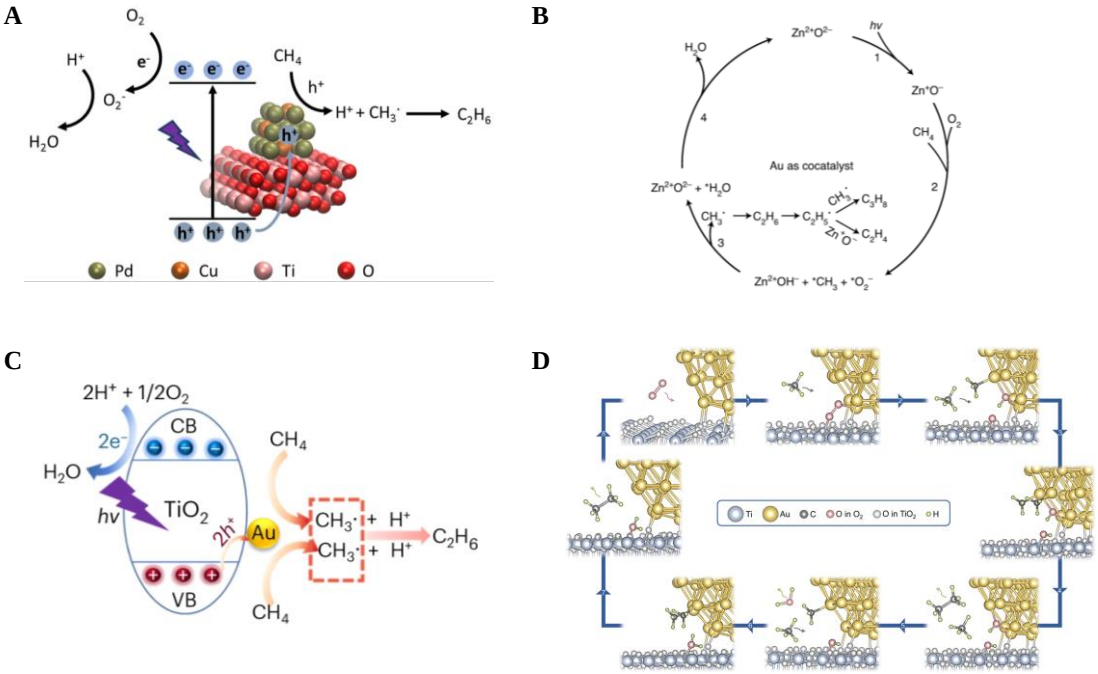

Figure 7. (**A**) Schematic diagram of photoexcitation and reaction over $PdCu/TiO_2$ [74]. (**B**) Schematic illustration of the reaction pathways for photocatalytic OCM over $Au–ZnO/TiO_2$(4/1) [76]. (**C**) Proposed POCM process over $Au60s/TiO_2$ [78]. (**D**) Schematic illustration of the proposed mechanism for photocatalytic OCM on $Au_{2.0\%}/TiO_2$ [79].

4. Photochemical Looping

Chemical looping involves decomposing a reaction into multiple sub-reactions, which are carried out in isolated spaces to achieve in situ separation of products [80–83]. In methane aerobic conversion reactions, the use of oxygen can lead to deep oxidation of methane and poses an explosion risk, significantly limiting the industrial application of this reaction. Applying chemical looping techniques to methane conversion, dividing the reaction into two half-reactions, can greatly improve the selectivity and safety of the reaction. This technology typically uses metal oxides as oxygen carriers. In the methane oxidation reaction, lattice oxygen is used instead of traditional O_2. Subsequently, the reduced oxygen carrier reacts with air to replenish the lattice oxygen, completing one reaction loop. Yong Lu's research team achieved methane oxidative coupling at lower temperatures through chemical looping to activate O_2 [84]. They developed a TiO_2-doped $Mn_2O_3–Na_2WO_4/SiO_2$ catalyst system, generating $MnTiO_3$ in the reaction flow, triggering the $MnTiO_3 \leftrightarrow Mn_2O_3$ chemical loop to activate O_2, achieving a 22% CH_4 conversion rate and 62% $C_2–C_3$ selectivity at 650 °C. Liang-Shih Fan's research team embedded Fe_2O_3 nanoparticles in a mesoporous SiO_2 carrier (Fe_2O_3@SBA-15), significantly suppressing CO_2 production in methane partial oxidation, achieving nearly 100% CO selectivity in a cyclic redox system at 750–935 °C [85]. Theoretical calculations indicated that low-coordination Fe atoms favored CH_4 adsorption and activation, while low-coordination lattice oxygen atoms significantly promoted Fe–O bond cleavage and CO formation, thereby enhancing CO selectivity.

Based on the characteristics of chemical looping, researchers have applied it to photocatalytic systems, yielding valuable results. In 2012, Jiesheng Chen's research team first reported a Ga^{3+}-modified ETS-10 molecular sieve material that utilized its oxygen centers and metal center active sites for strong activation of methane C—H bonds, achieving efficient coupling of methane to ethane at room temperature [86]. Under light irradiation, photogenerated electrons reduced Ti^{4+} to Ti^{3+}, while photogenerated holes oxidized surface hydroxyl groups to hydroxyl radicals, thus activating the C—H bonds of methane. As the reaction proceeded, Ti–OH groups were gradually consumed, leading to catalyst deactivation, which could be restored to photocatalytic activity by simple heat treatment in humid air.

In 2020, Khodakov's research team proposed a photochemical looping strategy using highly dispersed silver ions in a silver-phosphotungstic acid-titanium dioxide nanocomposite ($Ag–HPW/TiO_2$) to achieve high selectivity and nearly quantitative ethane production [87]. As Ag^+ was continuously reduced to metallic Ag, the catalyst's color changed from light gray to deep black, gradually deactivating the catalyst. To continuously synthesize ethane, the

catalyst was regenerated by exposing it to air under light for 7 h. As shown in Figure 8A, under light irradiation, the photocatalyst generated photogenerated electrons and holes. The electrons reduced Ag^+ to metallic Ag, while the holes oxidized CH_4 to $\cdot CH_3$, which coupled to form C_2H_6. Exposing the catalyst to air under light regenerated Ag to its oxidized state, forming an $Ag^+ \leftrightarrow Ag^0$ redox loop. This strategy separated the CH_4 oxidation step from the O_2 reduction step, effectively inhibiting methane overoxidation.

Similarly, Yongfu Sun's research team achieved efficient $CH_4 \rightarrow C_2H_6$ photocatalytic conversion using Au/ZnO porous nanosheets with dual active species of $Au^{\delta-}$ and O^- [88]. During photoexcitation, lattice oxygen in ZnO was easily oxidized to O^- active species. The generated $Au^{\delta-}$ and O^- could polarize the inert C—H bond and stabilize the resulting active $*CH_3$ intermediate, thus avoiding overoxidation. The consumed lattice oxygen was replenished through the Mars-van Krevelen mechanism. Ye Wang's research team constructed a solar-driven Fe^{3+}/Fe^{2+} redox loop, combining CH_4 photochemical coupling with electrochemical H_2 production. This system achieved high selectivity for CH_4 coupling to C_2H_6 while reducing the potential for electrochemical hydrogen production [89]. Fe^{3+} hydrolyzed to form $[Fe(H_2O)_5OH]^{2+}$, which absorbed UV light, transferring electrons from the OH to Fe^{3+}, resulting in free *OH and Fe^{2+}. *OH oxidized CH_4 to $*CH_3$, which coupled to form C_2H_6. Fe^{2+} was oxidized back to Fe^{3+} at the anode, replacing the traditional oxygen evolution reaction (OER), and H_2 was produced at the cathode, completing the redox loop (Figure 8B).

Yujie Xiong's research team proposed a methoxy- and ethoxy-intermediate-mediated pathway, directly photocatalytically converting CH_4 to C_2H_4 under mild conditions using $ZnO{-}AuPd_{2.7\%}$ [90]. Zn sites on ZnO served as the adsorption and activation sites for CH_4, activating it to $*CH_3$. The resulting $*CH_3$ preferred to combine with ZnO lattice oxygen to form methoxy intermediates. Assisted by Pd, methoxy could dehydrogenate to $-CH_2O$, which then reacted with another activated CH_4 to form ethoxy intermediates. Ethoxy further dehydrogenated to form C_2H_4, avoiding the overoxidation of CH_4 to CO_x. After 8 h, 3.68% of ZnO total lattice oxygen was consumed, reducing catalytic activity. The formed oxygen vacancies were easily replenished by washing with water. They also designed Pd−Zn modified WO_3 nanosheets ($Pd_5/Zn_{0.35}{-}WO_3$) to achieve efficient conversion of CH_4 to C_2H_4 [91]. Zn sites promoted the adsorption and activation of CH_4, forming methyl and methoxy intermediates with the help of lattice oxygen. Pd sites facilitated methoxy dehydrogenation to methylene radicals, forming C_2H_4 and inhibiting overoxidation. The consumed lattice oxygen could be replenished by photochemical looping with air exposure. Additionally, they reported a Pd single-atom modified TiO_2 photocatalyst (Pd_1/TiO_2) for methane coupling to ethane [92]. For TiO_2, the significant contribution of O atoms to the valence band made lattice oxygen directly involved in methane activation. The activated $*CH_3$ was difficult to desorb from O sites, leading to overoxidation. In Pd_1/TiO_2, the $Pd{-}O_4$ unit contributed most to the surface TiO_2 valence band maximum (VBM), accumulating photogenerated holes and facilitating CH_4 dissociation on Pd, inhibiting overoxidation with lattice oxygen. However, this process still required lattice oxygen consumption, leading to performance degradation after 6 h. The consumed lattice oxygen could be replenished by heating in air. Recently, they loaded Au NPs on $Nb_3O_7(OH)$ with abundant surface lattice hydroxyl groups, achieving efficient photocatalytic coupling of CH_4 to C_2H_6 under mild conditions [93]. Lattice hydroxyls on $Nb_3O_7(OH)$ facilitated CH_4 activation, forming key methoxy intermediates. The consumed lattice oxygen could be replenished by photochemical looping, either by washing with water or air exposure.

Photochemical looping strategies can also be applied to the partial oxidation of methane to produce oxygenates. In 2019, Khodakov's research team highly dispersed zinc on phosphotungstic acid/titanium dioxide ($Zn{-}HPW/TiO_2$), selectively photocatalytically oxidizing methane to carbon monoxide under ambient conditions [94]. Under UV excitation, ZnO formed $Zn^+{-}O^-$ pairs that adsorbed and activated methane to form Zn-methyl species. Surface methyl zinc reacted with zinc carbonate (formed from ZnO and gas-phase CO_2) to form methyl zinc carbonate, which decomposed to produce CO. After 12 h, the formation rates of CO and CO_2 slowed due to insufficient oxygen content and gradual reduction of Zn^{2+} to Zn^0. The Zn^{2+} was regenerated and lattice oxygen replenished through the Mars-van Krevelen mechanism by irradiation in air. Photochemical looping can also occur in gas-solid-liquid systems. Yujie Xiong's research team constructed a $PdO/Pd{-}WO_3$ heterojunction nanocomposite with CH_4 activation and C—C coupling active sites, directly converting CH_4 to CH_3COOH without introducing additional carbon sources [95]. As shown in Figure 8C, CH_4 adsorbed on Pd sites was activated by $\cdot OH$, with $*CH_3$ gradually converting to Pd−CO intermediates under the assistance of O atoms in PdO and $\cdot OH$ dehydrogenation. *CO and $*CH_3$ coupled to form $Pd{-}COCH_3$ intermediates, which further hydrolyzed to CH_3COOH. The formation of CH_3COOH consumed lattice oxygen in PdO, leading to performance decay after 3 h. The consumed lattice oxygen could be replenished by heating in air.

Currently, photochemical looping strategies for methane conversion are applied only in closed systems and not connected to air systems. Most applications are limited to batch systems. Future research should focus on reactor design, especially flow reaction systems. Additionally, the time-consuming Mars-van Krevelen mechanism for catalyst

regeneration needs to be made more efficient for industrial applications. Moreover, hydrogen products are mostly water. Adjusting the reaction pathways of active species to produce more valuable hydrogen gas would be beneficial. Combining photochemical looping strategies with methane conversion could solve existing challenges and realize the industrialization of photocatalytic methane conversion.

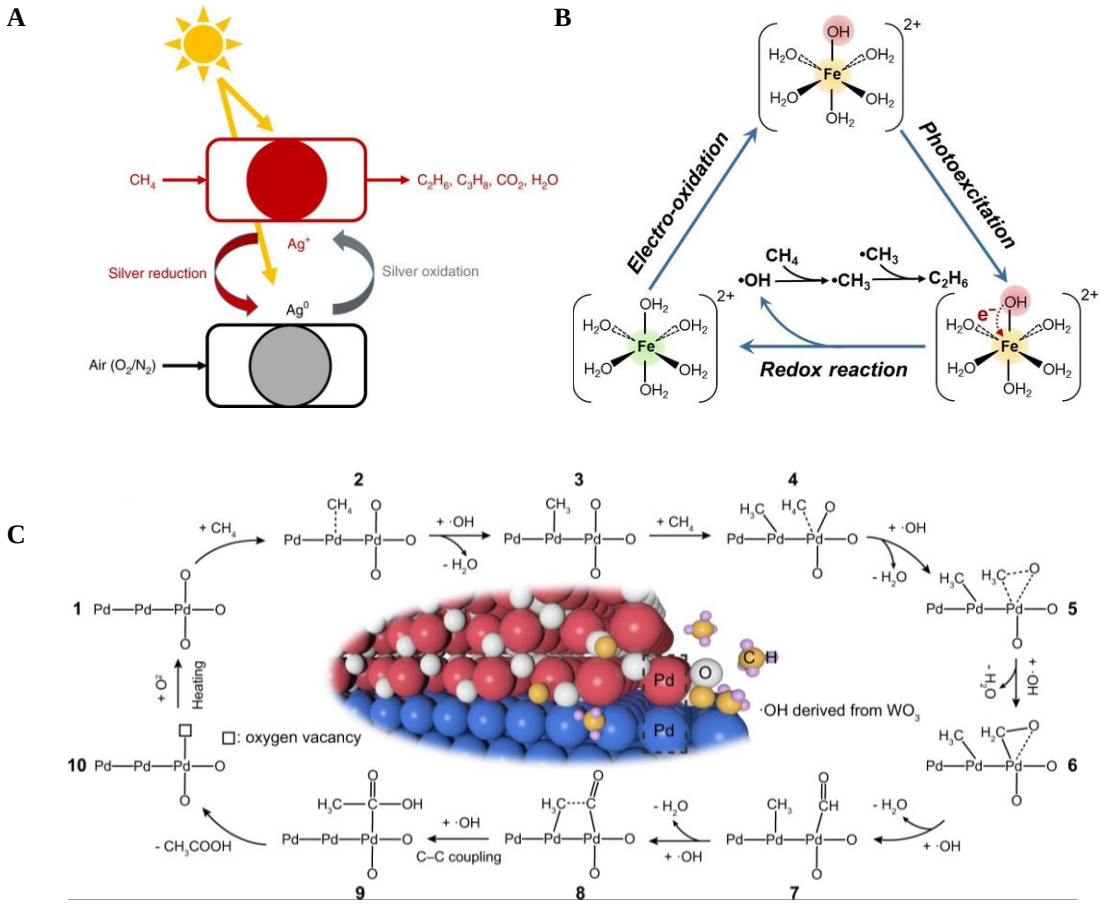

Figure 8. (**A**) Schematic diagram of a photochemical looping process on Ag−HPW/TiO_2 [87]. (**B**) Schematic diagram of the Fe^{3+}−Fe^{2+} cycle pathway and mechanism [89]. (**C**) Schematic illustration for photochemical conversion of CH_4 to CH_3COOH over PdO/Pd−WO_3 [95].

5. Summary and Outlook

Directly converting methane into value-added chemicals offers a promising alternative to the energy-intensive industrial methane reforming processes. Compared to the thermodynamically unfavorable non-oxidative coupling of methane (NOCM), the introduction of oxygen not only lowers the Gibbs free energy of the reaction, making it spontaneous, but also produces various reactive oxygen species that facilitate methane activation. Photocatalysis can reduce the activation barrier for methane, activating the inert C—H bond and enabling the reaction under milder conditions. This review has summarized the latest research progress in the photocatalytic partial oxidation of methane (PPOM) and oxidative coupling of methane (POCM) using oxygen as an oxidant. It primarily covers the activation mechanisms of methane and oxygen in different reaction systems, evaluation of methane aerobic conversion efficiency, and elucidation of reaction mechanisms. Additionally, the unique advantages of photochemical cycling in methane conversion are introduced. These insights aim to deepen the understanding of methane and oxygen activation mechanisms to design more efficient catalysts and reaction systems.

Despite substantial progress in photocatalytic methane conversion, significant gaps remain before industrial application can be realized. For example, the catalytic performance obtained experimentally is far from the requirements of industrial production; the high-carbon products is difficult to be synthesized efficiently and directionally; the poor selectivity of the products caused by peroxidation makes it difficult to separate the products; the reaction system is relatively elementary and the reactor is difficult to scale up; the studies of the reaction mechanism is insufficient, especially the activation mechanism of the C—H bond as well as the monitoring of the reaction intermediates and the reactive oxygen species. To address these issues, future research should focus on the following aspects:

(1) Designing Efficient Catalysts: Currently, most photocatalysts for methane conversion are UV-responsive. Therefore, designing narrow-bandgap semiconductors or black photocatalysts that absorb the entire solar spectrum, including visible and infrared light, is essential. Photocatalysts should also possess good electron-hole separation capabilities and suitable redox potentials. They should have moderate oxidation ability for methane and strong activation capacity for oxygen to promote the formation of reactive oxygen species. Typically, precious metals are introduced as cocatalysts to promote charge separation and oxygen activation. However, for economic viability, doping, defect engineering, heterojunction construction, or developing non-precious metal catalysts to replace precious metal catalysts should be explored. Traditional inorganic semiconductor materials often limit photocatalysts, so developing new photocatalytic materials, including covalent organic frameworks and inorganic-organic or metal-organic frameworks, may show excellent performance in methane conversion. Moreover, hot-carrier mediated photocatalysis can be induced by the Landau damping of surface plasmon resonance (SPR) in plasmonic metals or direct interband electron transitions in other noble metals [96,97]. Hot carriers can not only undergo relaxation to increase the catalyst surface temperature, but also directly participate in the photochemical reaction process, which greatly promotes the reaction efficiency. Therefore, by establishing a plasmonic or non-plasmonic hot carrier-based photocatalytic system can make isolating support materials exhibit photocatalytic activity, which undoubtedly enriches the photocatalyst system and has significant meaning for finding new photocatalyst materials.

(2) Hot carriers' effect: The role of metal nanoparticles is usually considered to be the promotion of light absorption, charge separation, activation of reactants, and stabilization of reaction intermediates. However, metal nanoparticles can simultaneously utilize the photo and thermal energy to promote reaction. The hot carriers' effect induced by metal nanoparticles should not be ignored for photocatalytic conversion of methane. More attention should be paid to how the hot carriers' effect promotes the reduction of O_2 and the activation of CH_4 to improve the efficiency and selectivity of the reaction. The electromagnetic decay of localized surface plasmon resonance (LSPR) on plasmonic nanoparticles such as Au, Ag and Cu or interband electron transition from the d-band to the s-band in non-plasmonic nanoparticles such as Pt, Pd, Rh, and Ru can produce hot carriers, which are different from those carriers generated by traditional semiconductor bandgap excitation [98,99]. In general, bandgap excitation and hot carrier generation compete with each other. Therefore, it is possible to promote the generation of hot carriers by choosing a suitable metal as well as by regulating the supports. Hot carrier relaxation can induce a photothermal effect to increase the catalyst surface temperature. Moreover, hot carriers can directly interact with gas molecules adsorbed on the surface of metal nanoparticles and thus participate in photochemical processes. Meanwhile, the process of hot carrier charge separation not only prolongs the carrier lifetime, but also promotes the reduction of O_2 and the activation of CH_4, which further improves the efficiency and selectivity of the reaction. Therefore, it is necessary to fully understand and utilize the hot carriers' effect of metal nanoparticles.

(3) Expanding to C_{2+} Products: The products of photocatalytic methane aerobic conversion are mostly C_1 oxygenates or C_2H_6, which have low commercial value and require further conversion for industrial significance. Reports on C_2 oxygenates, C_2H_4, and C_3H_8 are rare and yields are low. Methane activation energy is usually higher than that of oxidation products, leading to overoxidation of products. Oxidation and coupling reactions compete, making it challenging to form C_{2+} products. This necessitates deeper mechanistic studies to reveal possible reaction pathways and precise control of reaction sites and intermediates to promote C—C bond coupling.

(4) Developing Efficient Reaction Systems: The reaction system is critical for reaction activity and product selectivity. Although flow systems have advantages over batch systems in terms of gas-solid or gas-solid-liquid mass transfer efficiency, reaction stability, and selectivity, the complexity of methane conversion and the costs and safety of reactions should be considered. Drawing from mature flow systems in thermal catalysis, developing novel photocatalytic flow reactors is essential. Currently reported photocatalytic methane conversion flow systems mainly apply to gas-solid two-phase reactions. Gas-liquid-solid three-phase systems, such as those in methane partial oxidation, largely remain in batch reactors. Developing new reactors, such as membrane reactors, can further enhance methane reaction efficiency and target product selectivity. Reaction temperature, pressure, flow rate, CH_4/O_2 ratio, light source, and reaction time all affect yield and product selectivity. For example, an appropriate CH_4/O_2 ratio can prevent overoxidation in methane coupling, and pressurized reactors can increase the solubility of CH_4 and O_2 in H_2O. Additionally, due to the low selectivity of products in methane aerobic conversion, the cost of subsequent product separation is high. Rationally designing porous metal-organic frameworks can replace energy-intensive distillation for separation and purification.

(5) Utilizing Advanced In Situ Characterization: Research on the reaction mechanisms of photocatalytic methane aerobic conversion heavily relies on molecular and atomic-level characterization techniques, especially in situ and

operando characterization. Since oxygen activation can produce various reactive oxygen species, in situ EPR can detect these species to understand the mechanism of O_2 activation. Isotope labeling can determine the source of liquid oxygen. Advanced techniques like in situ IR spectroscopy, in situ XPS, and X-ray absorption spectroscopy can characterize the chemical states of reaction intermediates and active sites. Time-resolved spectroscopy can provide precise information on methane activation and conversion processes. Theoretical calculations can simulate reaction processes at the molecular level, exploring the reaction mechanism of methane conversion and determining the energies of different reaction steps, thus revealing the correct reaction pathway to guide the development of high-performance photocatalytic methane conversion systems.

In summary, abundant and inexpensive methane not only holds the potential to replace petroleum and other fossil fuels but can also serve as a raw material for synthesizing value-added chemicals. Due to methane's stability, activating and converting methane molecules is highly challenging. Activating methane's inert C—H bond using solar energy is strategically significant for energy development and sunlight utilization. Although there is still a gap between photocatalytic methane conversion and industrial application, achieving this will bring immense benefits to society.

Author Contributions

Conceptualization, Y.K. and L.L.; Methodology, Y.K.; Writing—Original Draft Preparation, Y.K. and C.Y.; Writing—Review & Editing, X.M. and L.L.; Project Administration, X.M., Y.C. and L.L.; Funding Acquisition, L.L.

Ethics Statement

Not applicable.

Informed Consent Statement

Not applicable.

Funding

This work was financially supported by the Natural Science Foundation of Jilin Province (grant nos. 20240101177JC and 20240302098GX), the National Natural Science Foundation (NSFC) of China (grant no. 22379050), the National Key Research and Development Program of China (2023YFA1506303), and the Fundamental Research Funds for the Central Universities.

Declaration of Competing Interest

The authors declare that they have no known competing financial interests or personal relationships that could have appeared to influence the work reported in this paper.

References

1. Schwach P, Pan X, Bao X. Direct Conversion of Methane to Value-Added Chemicals over Heterogeneous Catalysts: Challenges and Prospects. *Chem. Rev.* **2017**, *117*, 8497–8520.
2. Gunsalus NJ, Koppaka A, Park SH, Bischof SM, Hashiguchi BG, Periana RA. Homogeneous Functionalization of Methane. *Chem. Rev.* **2017**, *117*, 8521–8573.
3. Ma Z, Chen Y, Gao C, Xiong Y. A Minireview on the Role of Cocatalysts in Semiconductor-Based Photocatalytic CH_4 Conversion. *Energy Fuels* **2022**, *36*, 11428–11442.
4. Schwarz H. Chemistry with Methane: Concepts Rather than Recipes. *Angew. Chem. Int. Ed.* **2011**, *50*, 10096–10115.
5. Kang Y, Tian P, Li J, Wang H, Feng K. Methane mitigation potentials and related costs of China's coal mines. *Fundam. Res.* **2023**. https://doi.org/10.1016/j.fmre.2023.09.012.
6. Jiang Y, Li S, Fan X, Tang Z. Recent advances on aerobic photocatalytic methane conversion under mild conditions. *Nano Res.* **2023**, *16*, 12558–12571.
7. Baltrusaitis J, Jansen I, Schuttlefield Christus JD. Renewable energy based catalytic CH_4 conversion to fuels. *Catal. Sci. Technol.* **2014**, *4*, 2397–2411.
8. Zhan Q, Kong Y, Wang X, Li L. Photocatalytic non-oxidative conversion of methane. *Chem. Commun.* **2024**, *60*, 2732–2743.
9. Song H, Meng X, Wang Z-j, Liu H, Ye J. Solar-Energy-Mediated Methane Conversion. *Joule* **2019**, *3*, 1606–1636.

10. Wang P, Zhang X, Shi R, Zhao J, Yuan Z, Zhang T. Light-Driven Hydrogen Production from Steam Methane Reforming via Bimetallic PdNi Catalysts Derived from Layered Double Hydroxide Nanosheets. *Energy Fuels* **2022**, *36*, 11627–11635.
11. Mu X, Li L. Photo-Induced Activation of Methane at Room Temperature. *Acta Phys. -Chim. Sin.* **2019**, *35*, 968–976.
12. Angeli SD, Monteleone G, Giaconia A, Lemonidou AA. State-of-the-art catalysts for CH_4 steam reforming at low temperature. *Int. J. Hydrogen Energy* **2014**, *39*, 1979–1997.
13. Khodakov AY, Chu W, Fongarland P. Advances in the Development of Novel Cobalt Fischer-Tropsch Catalysts for Synthesis of Long-Chain Hydrocarbons and Clean Fuels. *Chem. Rev.* **2007**, *107*, 1692–1744.
14. Behrens M, Studt F, Kasatkin I, Kühl S, Hävecker M, Abild-Pedersen F, et al. The Active Site of Methanol Synthesis over $Cu/ZnO/Al_2O_3$ Industrial Catalysts. *Science* **2012**, *336*, 893–897.
15. Ab Rahim MH, Armstrong RD, Hammond C, Dimitratos N, Freakley SJ, Forde MM, et al. Low temperature selective oxidation of methane to methanol using titania supported gold palladium copper catalysts. *Catal. Sci. Technol.* **2016**, *6*, 3410–3418.
16. Agarwal N, Freakley SJ, McVicker RU, Althahban SM, Dimitratos N, He Q, et al. Aqueous Au−Pd colloids catalyze selective CH_4 oxidation to CH_3OH with O_2 under mild conditions. *Science* **2017**, *358*, 223–227.
17. Deng J, Chen P, Xia S, Zheng M, Song D, Lin Y, et al. Advances in Oxidative Coupling of Methane. *Atmosphere* **2023**, *14*, 1538.
18. Xu Y, Bao X, Lin L. Direct conversion of methane under nonoxidative conditions. *J. Catal.* **2003**, *216*, 386–395.
19. Liu J, Yue J, Lv M, Wang F, Cui Y, Zhang Z, et al. From fundamentals to chemical engineering on oxidative coupling of methane for ethylene production: A review. Carbon Resour. *Convers.* **2022**, *5*, 1–14.
20. Xu Y, Chen E, Tang J. Photocatalytic methane conversion to high-value chemicals. *Carbon Future* **2024**, *1*, 9200004.
21. Zhang L, Liu L, Pan Z, Zhang R, Gao Z, Wang G, et al. Visible-light-driven non-oxidative dehydrogenation of alkanes at ambient conditions. *Nat. Energy* **2022**, *7*, 1042–1051.
22. Tan R, Wang X, Kong Y, Ji Q, Zhan Q, Xiong Q, et al. Liberating C—H Bond Activation: Achieving 56% Quantum Efficiency in Photocatalytic Cyclohexane Dehydrogenation. *J. Am. Chem. Soc.* **2024**, *146*, 14149–14156.
23. Li L, Mu X, Liu W, Mi Z, Li C-J. Simple and Efficient System for Combined Solar Energy Harvesting and Reversible Hydrogen Storage. *J. Am. Chem. Soc.* **2015**, *137*, 7576–7579.
24. Li L, Li G-D, Yan C, Mu X-Y, Pan X-L, Zou X-X, et al. Efficient Sunlight-Driven Dehydrogenative Coupling of Methane to Ethane over a Zn^+-Modified Zeolite. *Angew. Chem. Int. Ed.* **2011**, *50*, 8299–8303.
25. Li L, Fan S, Mu X, Mi Z, Li C-J. Photoinduced Conversion of Methane into Benzene over GaN Nanowires. *J. Am. Chem. Soc.* **2014**, *136*, 7793–7796.
26. Zhang J, Shen J, Li D, Long J, Gao X, Feng W, et al. Efficiently Light-Driven Nonoxidative Coupling of Methane on Ag/$NaTaO_3$: A Case for Molecular-Level Understanding of the Coupling Mechanism. *ACS Catal.* **2023**, *13*, 2094–2105.
27. Wang G, Mu X, Li J, Zhan Q, Qian Y, Mu X, et al. Light-Induced Nonoxidative Coupling of Methane Using Stable Solid Solutions. *Angew. Chem. Int. Ed.* **2021**, *60*, 20760–20764.
28. Wang G, Mu X, Tan R, Pan Z, Li J, Zhan Q, et al. Fabrication of Stepped CeO_2 Nanoislands for Efficient Photocatalytic Methane Coupling. *ACS Catal.* **2023**, *13*, 11666–11674.
29. Kaliaguine SL, Shelimov BN, Kazansky VB. Reactions of methane and ethane with hole centers O^-. *J. Catal.* **1978**, *55*, 384–393.
30. Wang P, Shi R, Zhao J, Zhang T. Photodriven Methane Conversion on Transition Metal Oxide Catalyst: Recent Progress and Prospects. *Adv. Sci.* **2024**, *11*, 2305471.
31. Yang Z, Zhang Q, Song H, Chen X, Cui J, Sun Y, et al. Partial oxidation of methane by photocatalysis. *Chin. Chem. Lett.* **2024**, *35*, 108418.
32. Song H, Ye J. Direct photocatalytic conversion of methane to value-added chemicals. *Trends Chem.* **2022**, *4*, 1094–1105.
33. Ward MD, Brazdil JF, Mehandru SP, Anderson AB. Methane photoactivation on copper molybdate: An experimental and theoretical study. *J. Phys. Chem.* **2002**, *91*, 6515–6521.
34. Chen X, Li S. Photooxidation of Methane to Methanol by Molecular Oxygen on Water-preadsorbed Porous TiO_2-based Catalysts. *Chem. Lett.* **2000**, *29*, 314–315.
35. Li Y, Li J, Zhang G, Wang K, Wu X. Selective Photocatalytic Oxidation of Low Concentration Methane over Graphitic Carbon Nitride-Decorated Tungsten Bronze Cesium. *ACS Sustain. Chem. Eng.* **2019**, *7*, 4382–4389.
36. Thampi KR, Kiwi J, Grtzel M. Room temperature photo-activation of methane on TiO_2 supported molybdena. *Catal. Lett.* **1988**, *1*, 109–116.
37. Zhai J, Zhou B, Wu H, Jia S, Chu M, Han S, et al. Selective photocatalytic aerobic oxidation of methane into carbon monoxide over $Ag/AgCl@SiO_2$. *Chem. Sci.* **2022**, *13*, 4616–4622.

38. Jiang H, Peng X, Yamaguchi A, Ueda S, Fujita T, Abe H, et al. Photocatalytic Partial Oxidation of Methane on Palladium-Loaded Strontium Tantalate. *Sol. RRL* **2019**, *3*, 190076.
39. Jiang H, Peng X, Yamaguchi A, Fujita T, Abe H, Miyauchi M. Synergistic photothermal and photochemical partial oxidation of methane over noble metals incorporated in mesoporous silica. *Chem. Commun.* **2019**, *55*, 13765–13768.
40. Dong C, Hu D, Ben Tayeb K, Simon P, Addad A, Trentesaux M, et al. Photocatalytic partial oxidation of methane to carbon monoxide and hydrogen over CIGS solar cell. *Appl. Catal. B Environ.* **2023**, *325*, 122340.
41. Song H, Meng X, Wang S, Zhou W, Wang X, Kako T, et al. Direct and Selective Photocatalytic Oxidation of CH_4 to Oxygenates with O_2 on Cocatalysts/ZnO at Room Temperature in Water. *J. Am. Chem. Soc.* **2019**, *141*, 20507–20515.
42. Song H, Meng X, Wang S, Zhou W, Song S, Kako T, et al. Selective Photo-oxidation of Methane to Methanol with Oxygen over Dual-Cocatalyst-Modified Titanium Dioxide. *ACS Catal.* **2020**, *10*, 14318–14326.
43. Luo L, Gong Z, Xu Y, Ma J, Liu H, Xing J, et al. Binary Au−Cu Reaction Sites Decorated ZnO for Selective Methane Oxidation to C_1 Oxygenates with Nearly 100% Selectivity at Room Temperature. *J. Am. Chem. Soc.* **2021**, *144*, 740–750.
44. Luo L, Fu L, Liu H, Xu Y, Xing J, Chang C-R, et al. Synergy of Pd atoms and oxygen vacancies on In_2O_3 for methane conversion under visible light. *Nat. Commun.* **2022**, *13*, 2930.
45. Gong Z, Luo L, Wang C, Tang J. Photocatalytic Methane Conversion to C_1 Oxygenates over Palladium and Oxygen Vacancies Co-Decorated TiO_2. Sol. *RRL* **2022**, *6*, 2200335.
46. Wang K, Luo L, Wang C, Tang J. Photocatalytic methane activation by dual reaction sites co-modified WO_3. Chin. *J. Catal.* **2023**, *46*, 103–112.
47. Luo L, Han X, Wang K, Xu Y, Xiong L, Ma J, et al. Nearly 100% selective and visible-light-driven methane conversion to formaldehyde via. single-atom Cu and $W^{\delta+}$. *Nat. Commun.* **2023**, *14*, 2690.
48. Chen F, Zhou H, Liu D, Qin X, Jing Y, Chen L, et al. Defective ZnO Nanoplates Supported AuPd Nanoparticles for Efficient Photocatalytic Methane Oxidation to Oxygenates. *Adv. Energy Mater.* **2024**, *14*, 2303642.
49. Jiang Y, Li S, Wang S, Zhang Y, Long C, Xie J, et al. Enabling Specific Photocatalytic Methane Oxidation by Controlling Free Radical Type. *J. Am. Chem. Soc.* **2023**, *145*, 2698–2707.
50. Zhou W, Qiu X, Jiang Y, Fan Y, Wei S, Han D, et al. Highly selective aerobic oxidation of methane to methanol over gold decorated zinc oxide via photocatalysis. *J. Mater. Chem. A* **2020**, *8*, 13277–13284.
51. Fan Y, Zhou W, Qiu X, Li H, Jiang Y, Sun Z, et al. Selective photocatalytic oxidation of methane by quantum-sized bismuth vanadate. *Nat. Sustain.* **2021**, *4*, 509–515.
52. Du X, Yang Z, Yang X, Zhang Q, Liu L, Ye J. Efficient Photocatalytic Conversion of Methane into Ethanol over P-Doped g-C_3N_4 under Ambient Conditions. *Energy Fuels* **2022**, *36*, 3929–3937.
53. An B, Zhang Qh, Zheng Bs, Li M, Xi Yy, Jin X, et al. Sulfone-Decorated Conjugated Organic Polymers Activate Oxygen for Photocatalytic Methane Conversion. *Angew. Chem. Int. Ed.* **2022**, *61*, e202204661.
54. Zhou Q, Tan X, Wang X, Zhang Q, Qi C, Yang H, et al. Selective Photocatalytic Oxidation of Methane to Methanol by Constructing a Rapid O_2 Conversion Pathway over Au–Pd/ZnO. *ACS Catal.* **2024**, *14*, 955–964.
55. Zhang X, Wang Y, Chang K, Yang S, Liu H, Chen Q, et al. Constructing hollow porous Pd/H−TiO_2 photocatalyst for highly selective photocatalytic oxidation of methane to methanol with O_2. *Appl. Catal. B Environ.* **2023**, *320*, 121961.
56. Huang M, Zhang S, Wu B, Yu X, Gan Y, Lin T, et al. Highly Selective Photocatalytic Aerobic Oxidation of Methane to Oxygenates with Water over W-doped TiO_2. *ChemSusChem* **2022**, *15*, e202200548.
57. Huang M, Zhang S, Wu B, Wei Y, Yu X, Gan Y, et al. Selective Photocatalytic Oxidation of Methane to Oxygenates over Cu−W−TiO_2 with Significant Carrier Traps. *ACS Catal.* **2022**, *12*, 9515–9525.
58. Huang M, Zhang S, Gan Y, Liu J, He Z, Lin T, et al. Effective $SrWO_4$/TiO_2 Heterojunction with Enhanced Carriers Separation and Transfer for Photocatalytic Methane Oxidation. *Chem. Eur. J.* **2023**, *29*, e202204031.
59. Cai X, Fang S, Hu YH. Unprecedentedly high efficiency for photocatalytic conversion of methane to methanol over Au–Pd/TiO_2−what is the role of each component in the system? *J. Mater. Chem. A* **2021**, *9*, 10796–10802.
60. Wei S, Zhu X, Zhang P, Fan Y, Sun Z, Zhao X, et al. Aerobic oxidation of methane to formaldehyde mediated by crystal-O over gold modified tungsten trioxide via photocatalysis. *Appl. Catal. B Environ.* **2021**, *283*, 119661.
61. Feng N, Lin H, Song H, Yang L, Tang D, Deng F, et al. Efficient and selective photocatalytic CH_4 conversion to CH_3OH with O_2 by controlling overoxidation on TiO_2. *Nat. Commun.* **2021**, *12*, 4652.
62. Jiang Y, Zhao W, Li S, Wang S, Fan Y, Wang F, et al. Elevating Photooxidation of Methane to Formaldehyde via TiO_2 Crystal Phase Engineering. *J. Am. Chem. Soc.* **2022**, *144*, 15977–15987.
63. Farrell BL, Igenegbai VO, Linic S. A Viewpoint on Direct Methane Conversion to Ethane and Ethylene Using Oxidative Coupling on Solid Catalysts. *ACS Catal.* **2016**, *6*, 4340–4346.

64. Keller GE, Bhasin MM. Synthesis of ethylene via oxidative coupling of methane: I. *Determination of active catalysts. J. Catal.* **1982**, *73*, 9–19.
65. Meng L, Chen Z, Ma Z, He S, Hou Y, Li H-H, et al. Gold plasmon-induced photocatalytic dehydrogenative coupling of methane to ethane on polar oxide surfaces. *Energy Environ. Sci.* **2018**, *11*, 294–298.
66. Wang P, Shi R, Zhao Y, Li Z, Zhao J, Zhao J, et al. Selective Photocatalytic Oxidative Coupling of Methane via Regulating Methyl Intermediates over Metal/ZnO Nanoparticles. *Angew. Chem. Int. Ed.* **2023**, *62*, e202304301.
67. Souza JD, Souza VS, Scholten JD. Synthesis of Hybrid Zinc-Based Materials from Ionic Liquids: A Novel Route to Prepare Active Zn Catalysts for the Photoactivation of Water and Methane. *ACS Sustain. Chem. Eng.* **2019**, *7*, 8090–8098.
68. Chai Y, Tang S, Wang Q, Wu Q, Liang J, Li L. Gold nanoparticles supported on $ZnGa_2O_4$ nanosheets as efficient photocatalysts for selective oxidation of methane to ethane under ambient conditions. *Appl. Catal. B Environ.* **2023**, *338*, 123012.
69. Fei M, Williams B, Wang L, Li H, Yuan Y, Wilkes JR, et al. Highly Selective Photocatalytic Methane Coupling by Au-Modified Bi_2WO_6. *ACS Catal.* **2024**, *14*, 1855–1861.
70. Zhang J, Zhang J, Shen J, Li D, Long J, Dai W, et al. Regulation of Oxygen Activation Pathways to Optimize Photocatalytic Methane Oxidative Coupling Selectivity. *ACS Catal.* **2024**, *14*, 3855–3866.
71. Sun X, Liu G, Shen T, Hu Y, Song Z, Wu Z, et al. Directional Activation of Oxygen by the Au-Loaded ZnAl-LDH with Defect Structure for Highly Efficient Photocatalytic Oxidative Coupling of Methane. *Small* **2024**. https://doi.org/10.1002/smll.202310857.
72. Li X, Xie J, Rao H, Wang C, Tang J. Platinum- and CuO_x-Decorated TiO_2 Photocatalyst for Oxidative Coupling of Methane to C_2 Hydrocarbons in a Flow Reactor. *Angew. Chem. Int. Ed.* **2020**, *59*, 19702–19707.
73. Yang J, Wang C, Xing J, Tang J. Palladium decorated anatase for photocatalytic partial oxidation of methane to ethane. *Surf. Interfaces* **2023**, *40*, 103108.
74. Li X, Wang C, Yang J, Xu Y, Yang Y, Yu J, et al. PdCu nanoalloy decorated photocatalysts for efficient and selective oxidative coupling of methane in flow reactors. *Nat. Commun.* **2023**, *14*, 6343.
75. Wang C, Li X, Ren Y, Jiao H, Wang FR, Tang J. Synergy of Ag and AgBr in a Pressurized Flow Reactor for Selective Photocatalytic Oxidative Coupling of Methane. *ACS Catal.* **2023**, *13*, 3768–3774.
76. Song S, Song H, Li L, Wang S, Chu W, Peng K, et al. A selective Au−ZnO/TiO_2 hybrid photocatalyst for oxidative coupling of methane to ethane with dioxygen. *Nat. Catal.* **2021**, *4*, 1032–1042.
77. Hu D, Dong C, Belhout S, Shetty S, Ng H, Brasseur P, et al. Roles of titania and plasmonic gold nanoparticles of different sizes in photocatalytic methane coupling at room temperature. *Mater. Today Energy* **2023**, *36*, 101358.
78. Li X, Li C, Xu Y, Liu Q, Bahri M, Zhang L, et al. Efficient hole abstraction for highly selective oxidative coupling of methane by Au-sputtered TiO_2 photocatalysts. *Nat. Energy* **2023**, *8*, 1013–1022.
79. Chen Y, Zhao Y, Liu D, Wang G, Jiang W, Liu S, et al. Continuous Flow System for Highly Efficient and Durable Photocatalytic Oxidative Coupling of Methane. *J. Am. Chem. Soc.* **2024**, *146*, 2465–2473.
80. Deng G, Li K, Gu Z, Zhu X, Wei Y, Cheng X, et al. Synergy effects of combined red muds as oxygen carriers for chemical looping combustion of methane. *Chem. Eng. J.* **2018**, *341*, 588–600.
81. Lambert A, Delquié C, Clémeneçon I, Comte E, Lefebvre V, Rousseau J, et al. Synthesis and characterization of bimetallic Fe/Mn oxides for chemical looping combustion. *Energy Procedia* **2009**, *1*, 375–381.
82. Zheng Y, Li K, Wang H, Zhu X, Wei Y, Zheng M, et al. Enhanced Activity of CeO_2−ZrO_2 Solid Solutions for Chemical-Looping Reforming of Methane via Tuning the Macroporous Structure. *Energy Fuels* **2016**, *30*, 638–647.
83. Haribal VP, Wang X, Dudek R, Paulus C, Turk B, Gupta R, et al. Modified Ceria for "Low-Temperature" CO_2 Utilization: A Chemical Looping Route to Exploit Industrial Waste Heat. *Adv. Energy Mater.* **2019**, *9*, 1901963.
84. Wang P, Zhao G, Wang Y, Lu Y. $MnTiO_3$-driven low-temperature oxidative coupling of methane over TiO_2-doped Mn_2O_3-Na_2WO_4/SiO_2 catalyst. *Sci. Adv.* **2017**, *3*, e1603180.
85. Liu Y, Qin L, Cheng Z, Goetze JW, Kong F, Fan JA, et al. Near 100% CO selectivity in nanoscaled iron-based oxygen carriers for chemical looping methane partial oxidation. *Nat. Commun.* **2019**, *10*, 5503.
86. Li L, Cai Y-Y, Li G-D, Mu X-Y, Wang K-X, Chen J-S. Synergistic Effect on the Photoactivation of the Methane C—H Bond over Ga^{3+}-Modified ETS-10. *Angew. Chem. Int. Ed.* **2012**, *51*, 4702–4706.
87. Yu X, Zholobenko VL, Moldovan S, Hu D, Wu D, Ordomsky VV, et al. Stoichiometric methane conversion to ethane using photochemical looping at ambient temperature. *Nat. Energy* **2020**, *5*, 511–519.
88. Zheng K, Zhang X, Hu J, Xu C, Zhu J, Li J, et al. High-rate CH_4-to-C_2H_6 photoconversion enabled by Au/ZnO porous nanosheets under oxygen-free system. *Sci. China Chem.* **2024**, *67*, 869–875.
89. Zhang H, Zhong W, Gong Q, Sun P, Fei X, Wu X, et al. Photo-Driven Iron-Induced Non-Oxidative Coupling of Methane to Ethane. *Angew. Chem. Int. Ed.* **2023**, *62*, e202303405.

90. Jiang W, Low J, Mao K, Duan D, Chen S, Liu W, et al. Pd-Modified ZnO−Au Enabling Alkoxy Intermediates Formation and Dehydrogenation for Photocatalytic Conversion of Methane to Ethylene. *J. Am. Chem. Soc.* **2021**, *143*, 269–278.
91. Liu Y, Chen Y, Jiang W, Kong T, Camargo PHC, Gao C, et al. Highly Efficient and Selective Photocatalytic Nonoxidative Coupling of Methane to Ethylene over Pd−Zn Synergistic Catalytic Sites. *Research* **2022**, *2022*, 9831340.
92. Zhang W, Fu C, Low J, Duan D, Ma J, Jiang W, et al. High-performance photocatalytic nonoxidative conversion of methane to ethane and hydrogen by heteroatoms-engineered TiO_2. *Nat. Commun.* **2022**, *13*, 2806.
93. Ma Z, Chen Y, Gao C, Xiong Y. Engineering surface lattice hydroxyl groups toward highly efficient photocatalytic methane coupling. *Chem. Commun.* **2024**, *60*, 1132–1135.
94. Yu X, De Waele V, Löfberg A, Ordomsky V, Khodakov AY. Selective photocatalytic conversion of methane into carbon monoxide over zinc-heteropolyacid-titania nanocomposites. *Nat. Commun.* **2019**, *10*, 700.
95. Zhang W, Xi D, Chen Y, Chen A, Jiang Y, Liu H, et al. Light-driven flow synthesis of acetic acid from methane with chemical looping. *Nat. Commun.* **2023**, *14*, 3047.
96. Clavero C. Plasmon-induced hot-electron generation at nanoparticle/metal-oxide interfaces for photovoltaic and photocatalytic devices. *Nat. Photonics* **2014**, *8*, 95–103.
97. Sarina S, Zhu H-Y, Xiao Q, Jaatinen E, Jia J, Huang Y, et al. Viable Photocatalysts under Solar-Spectrum Irradiation: Nonplasmonic Metal Nanoparticles. *Angew. Chem. Int. Ed.* **2014**, *53*, 2935–2940.
98. Aslam U, Rao VG, Chavez S, Linic S. Catalytic conversion of solar to chemical energy on plasmonic metal nanostructures. *Nat. Catal.* **2018**, *1*, 656–665.
99. Zhang Y, He S, Guo W, Hu Y, Huang J, Mulcahy JR, et al. Surface-Plasmon-Driven Hot Electron Photochemistry. *Chem. Rev.* **2018**, *118*, 2927–2954.